



Photocurable bioresorbable adhesives as functional interfaces between flexible bioelectronic devices and soft biological tissues

Quansan Yang^{1,2,3,26}, Tong Wei^{4,26}, Rose T. Yin^{5,26}, Mingzheng Wu^{6,26}, Yameng Xu^{7,8,26}, Jahyun Koo⁹, Yeon Sik Choi^{1,2,7}, Zhaoqian Xie^{10,11,12}, Sheena W. Chen¹³, Irawati Kandela^{14,15}, Shenglian Yao¹⁶, Yujun Deng^{3,17}, Raudel Avila³, Tzu-Li Liu³, Wubin Bai^{1,2,7,18}, Yiyuan Yang^{1,2,3}, Mengdi Han^{1,2}, Qihui Zhang⁷, Chad R. Haney^{15,19,20}, K. Benjamin Lee¹³, Kedar Aras¹⁵, Tong Wang^{15,19,20}, Min-Ho Seo^{1,2,7,21}, Haiwen Luan^{1,2,3}, Seung Min Lee⁷, Anil Brikha^{15,19}, Nayereh Ghoreishi-Haack¹⁴, Lori Tran^{14,15}, Iwona Stepień^{14,15}, Fraser Aird¹⁵, Emily A. Waters^{15,19,20}, Xinge Yu²², Anthony Banks^{1,2}, Gregory D. Trachiotis^{5,23}, John M. Torkelson^{4,7}, Yonggang Huang^{1,3,7,24}, Yevgenia Kozorovitskiy^{6,15}✉, Igor R. Efimov⁵✉ and John A. Rogers^{1,2,3,7,20,25}✉

Flexible electronic/optoelectronic systems that can intimately integrate onto the surfaces of vital organ systems have the potential to offer revolutionary diagnostic and therapeutic capabilities relevant to a wide spectrum of diseases and disorders. The critical interfaces between such technologies and living tissues must provide soft mechanical coupling and efficient optical/electrical/chemical exchange. Here, we introduce a functional adhesive bioelectronic-tissue interface material, in the forms of mechanically compliant, electrically conductive, and optically transparent encapsulating coatings, interfacial layers or supporting matrices. These materials strongly bond both to the surfaces of the devices and to those of different internal organs, with stable adhesion for several days to months, in chemistries that can be tailored to bioresorb at controlled rates. Experimental demonstrations in live animal models include device applications that range from battery-free optoelectronic systems for deep-brain optogenetics and subdermal phototherapy to wireless millimetre-scale pacemakers and flexible multi-electrode epicardial arrays. These advances have immediate applicability across nearly all types of bioelectronic/optoelectronic system currently used in animal model studies, and they also have the potential for future treatment of life-threatening diseases and disorders in humans.

Capabilities that follow from the intimate integration of high-performance electronic/optoelectronic systems with soft living tissues have the potential to serve as the basis for revolutionary approaches to diagnosing and treating diseases^{1–5}. A common vision is that a synergistic, bidirectional union of technology with biology will establish routes to improving health and

prolonging life in ways that could complement those of traditional techniques. In all cases, the physical interfaces between these abiotic and biotic systems must enable soft mechanical coupling and functional optical/electrical/chemical exchange^{6–8}. Structural techniques based on surgical sutures, staples, cuffs or clips⁹ have some utility but they induce damage to the tissues and the

¹Center for Bio-Integrated Electronics, Northwestern University, Evanston, IL, USA. ²Querrey Simpson Institute for Bioelectronics, Northwestern University, Evanston, IL, USA. ³Department of Mechanical Engineering, Northwestern University, Evanston, IL, USA. ⁴Department of Chemical and Biological Engineering, Northwestern University, Evanston, IL, USA. ⁵Department of Biomedical Engineering, The George Washington University, Washington, DC, USA. ⁶Department of Neurobiology, Northwestern University, Evanston, IL, USA. ⁷Department of Materials Science and Engineering, Northwestern University, Evanston, IL, USA. ⁸The Institute of Materials Science and Engineering, Washington University in St. Louis, St. Louis, MO, USA. ⁹School of Biomedical Engineering, Korea University, Seoul, Republic of Korea. ¹⁰State Key Laboratory of Structural Analysis for Industrial Equipment, Dalian University of Technology, Dalian, China. ¹¹Department of Engineering Mechanics, Dalian University of Technology, Dalian, China. ¹²Ningbo Institute of Dalian University of Technology, Ningbo, China. ¹³Department of Surgery, The George Washington University, Washington, DC, USA. ¹⁴Developmental Therapeutics Core, Northwestern University, Evanston, IL, USA. ¹⁵Chemistry Life Processes Institute, Northwestern University, Evanston, IL, USA. ¹⁶School of Materials Science and Engineering, University of Science and Technology Beijing, Beijing, China. ¹⁷State Key Laboratory of Mechanical System and Vibration, Shanghai Jiao Tong University, Shanghai, China. ¹⁸Department of Applied Physical Sciences, University of North Carolina at Chapel Hill, Chapel Hill, NC, USA. ¹⁹Center for Advanced Molecular Imaging, Northwestern University, Evanston, IL, USA. ²⁰Department of Biomedical Engineering, Northwestern University, Evanston, IL, USA. ²¹School of Biomedical Convergence Engineering, College of Information & Biomedical Engineering, Pusan National University, Pusan, Republic of Korea. ²²Department of Biomedical Engineering, City University of Hong Kong, Hong Kong, China. ²³DC Veterans Affairs Medical Center, The George Washington University, Washington, DC, USA. ²⁴Departments of Civil and Environmental Engineering, Northwestern University, Evanston, IL, USA. ²⁵Department of Neurological Surgery, Feinberg School of Medicine, Northwestern University, Chicago, IL, USA.

²⁶These authors contributed equally: Quansan Yang, Tong Wei, Rose T. Yin, Mingzheng Wu, Yameng Xu. ✉e-mail: yevgenia.kozorovitskiy@northwestern.edu; efimov@gwu.edu; jrogers@northwestern.edu

devices¹⁰, and they often result in adverse immune responses^{11,12} and mechanical instabilities. Such methods also support bonding only at discrete locations, leading to unreliable and/or inhomogeneous, time-varying contacts across the full interfacial area¹³. Existing adhesives for tissue repair^{14–18}, drug delivery¹⁴ and wound dressings¹⁹ may have utility, but these materials fail to satisfy all of the essential requirements for bioelectronic–tissue interfaces (detailed limitations in Supplementary Note 1 and Supplementary Tables 1 and 2). The adhesive must provide robust adhesion, not only to biological tissues, but also to the surfaces of electronic devices with mechanical, geometrical and chemical characteristics that are vastly different from those of the soft tissues. During the surgical process, the processes of applying and activating the interface materials must minimize deformation and damage to the tissues and the devices. Application must occur easily, across diverse classes of electronic systems, including those adopting three-dimensional (3D) layouts and/or complex surface topographical features²⁰. To support functional electronic or optical exchange between devices and tissues, high light transmission and appropriate levels of ionic conductivity are also important^{21–23}. For applications in transient electronics, the chemistries must accommodate designs that offer bioresorbability with rates that match use cases in temporary implants.

This paper introduces a functional adhesive, which we refer to as a bioelectronic–tissue interface material (BTIM), that meets the requirements outlined above. The BTIM combines photocurable covalent networks (polyethylene glycol–lactide acid diacrylate, PEG–LA–DA; Supplementary Fig. 1 and Supplementary Note 2) with ionic networks (sodium alginate, SA) that quickly form upon application to tissue–electronics surfaces. The result is a material with a honey-like initial viscosity that can flow to conform to complex surfaces. Chemical designs support robust bonding to both sides of the interface *in situ*. Conformal coverage across complex tissue–electronics surfaces enables multiple strategies to address diverse classes of biological tissues and electronic systems. Photopolymerization leads to a liquid–solid transformation and bonding without application of force, thereby facilitating surgical processes and reducing the potential for damage or excessive deformation of fragile tissues or delicate electronic devices. These BTIMs are highly transparent, with the electrical conductivity that arises from motions of ions in the network, to meet requirements for wide-ranging types of optoelectronic and bioelectronic device. The lactic acid units, along with the alginate and chitosan components, allow for complete controlled resorption in the body through natural processes at well defined rates, thereby addressing opportunities in temporary implants that are designed to eliminate costs and risks of surgical removal procedures.

An important component of this work is a collection of demonstrations with diverse electronic/optoelectronic devices interfaced to the surfaces of different vital organs in the context of optical and electronic modes of stimulation and measurement in live animal models, from days and weeks to months. Examples include battery-free optoelectronic platforms that wirelessly deliver light stimuli to regions of the deep brain or subcutaneous tissues, stably and without inciting inflammation. In other experiments, the BTIM forms adhesive ‘tunnels’, or conduits, for interconnects/cables that join different components of implantable devices to span large distances across the anatomy. Further demonstrations highlight applicability to highly dynamic organs such as the heart, where wireless millimetre-scale pacemakers and high-density flexible multielectrode arrays (MEAs) mount directly onto the epicardial surfaces of rat models and Langendorff-perfused rabbit hearts, respectively. All of these BTIM-assisted bioelectronic/optoelectronic devices retain their functions and positions throughout the periods of study. These collective results highlight the broad spectrum of possibilities enabled by this class of adhesive material.

BTIM designs and characterizations

Figure 1a presents a schematic illustration of the standard means for establishing interfaces by use of sutures, as a reference⁹ for the methods introduced here (illustrations in Fig. 1b–d), where thin, soft layers of the BTIM serve as soft, transparent and electrically conductive bonds to the targeted tissues. Suturing (Fig. 1a) typically requires multiple points of attachment via threads that penetrate the device and the tissue, thereby causing damage to both. The BTIM, by contrast, can be used as encapsulating coatings (Fig. 1b), interfacial layers (Fig. 1c) or supporting matrices (Fig. 1d), depending on the device architectures and application scenarios. The encapsulation technique involves casting and curing a liquid precursor of the BTIM onto the surface of a device to yield a coating that extends to the adjacent tissues. This scheme physically holds the device through chemical bonds formed with the surrounding tissue. In the interface method, the BTIM chemically bonds to the amine-functionalized bottom surface of the device on one side, and to the tissue on the other. In the matrix scheme, the precursor flows around the 3D structured device to form a solid, supportive and protective matrix that can be joined to the surface of the tissue using the other two approaches. Photographs associated with the application of this two-component adhesive chemistry to a porcine heart to anchor a pair of electrodes with the encapsulation coating scheme appear in Fig. 1e. As shown in Fig. 1f, Extended Data Fig. 1 and Supplementary Figs. 2 and 3, this material system allows seamless integration of electronic and optoelectronic systems, including 3D platforms, onto the surfaces of living tissues, with robust adhesion for stable electrical and/or optical interfaces across dermal, neuronal and cardiac applications for several days to months (detailed procedure in Supplementary Fig. 4).

Figure 2a presents the mechanisms of bonding to the surfaces of biological tissues (top) and devices (bottom) through the use of primers. The primer for the tissue surfaces¹⁵ consists of chitosan and coupling reagents (1-ethyl-3-(3-dimethylaminopropyl) carbodiimide (EDC) and sulfated *N*-hydroxysuccinimide (Sulfo-NHS)). The primary amine groups on the chitosan backbone covalently bond with carboxylic acid groups on the tissue surfaces and the alginate network to provide robust bonding, which is further enhanced by physical chain entanglement. The primer (EDC and Sulfo-NHS) for the devices promotes the reaction between amine groups functionalized onto device surfaces and carboxylic acid groups in the adhesive matrix. The amine groups (Supplementary Note 3) enable robust adhesion to the BTIM, with negligible influence on the device impedance (Extended Data Fig. 2).

The combined effects of high cohesion energy (1,900 J m⁻²; Supplementary Note 4 and Supplementary Fig. 5) and strong bonding lead to high levels of adhesion strength, capable of addressing requirements for a wide variety of tissues and devices (Fig. 2b and Supplementary Figs. 6 and 7). Examples of bonding to wet tissue surfaces include the skin (300 ± 70 J m⁻²), the epicardium (240 ± 20 J m⁻²), the gastrointestinal wall (80 ± 30 J m⁻²), the renal cortex (70 ± 10 J m⁻²) and the hepatic lobule (50 ± 10 J m⁻²). Bioelectronic surfaces include various encapsulation/substrate materials such as poly(lactic-co-glycolic acid) (PLGA; 260 ± 50 J m⁻²), polylactic acid (PLA; 250 ± 50 J m⁻²), polycaprolactone (240 ± 40 J m⁻²), parylene (120 ± 40 J m⁻²), polyimide (PI; 110 ± 30 J m⁻²) and polyurethane (90 ± 50 J m⁻²).

Low-modulus mechanical properties (Young’s modulus ~30 kPa) and high levels of elongation (up to tenfold) of the BTIM minimize stresses, and potential damage, at the tissue interfaces (Fig. 2c,d)^{24,25}. Here, the material serves as a soft, strain-isolation layer between devices and the tissues, with minimal normal and shear stresses associated with natural motions such as side-bending (angle 45°) and bending over (angle 75°) analysed by finite-element analysis (Fig. 2d and Supplementary Figs. 8 and 9). The strain-isolating effects of the BTIM (thickness 500 μm) decrease the stresses by a factor of up to

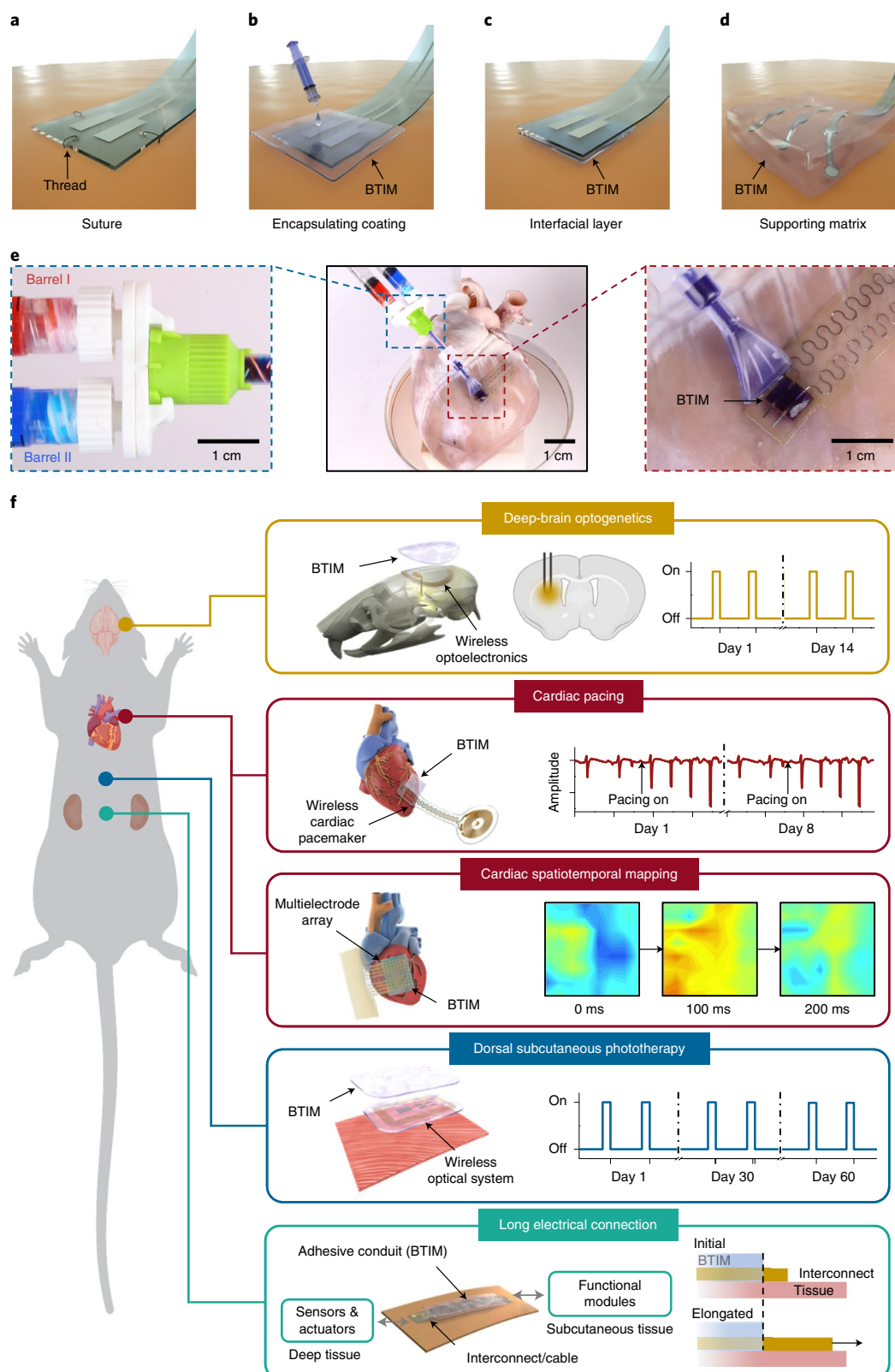


Fig. 1 | Soft interface materials for joining bioelectronic devices with biological tissues. **a–d**, Schematic illustrations of a conventional suturing process (**a**) and three alternative schemes based on the BTIM, including encapsulating coatings (**b**), interfacial layers (**c**) and supporting matrices (**d**). **e**, Procedures for applying this two-component adhesive chemistry to a porcine heart to anchor a pair of electrodes via the encapsulation scheme. Blue inset: precursors from barrel I (dyed red; PEG-LA-DA, Ca^{2+} and photoinitiators) and barrel II (dyed blue; SA) of a dual-syringe delivery system mix as they pass through the shaft and emerge at the tip end, highlighted in purple. Red inset: applying the resulting liquid mixture to tissue coated with primer, followed by curing into a solid form by exposure to UV light (wavelength 365 nm; density 20 mW cm^{-2} ; duration 3 min) to complete the encapsulation process. **f**, Seamless integration of electronic and optoelectronic systems onto the surfaces of living tissues, with robust adhesion for stable electrical and/or optical interfaces across dermal, neuronal and cardiac applications for several days to months.

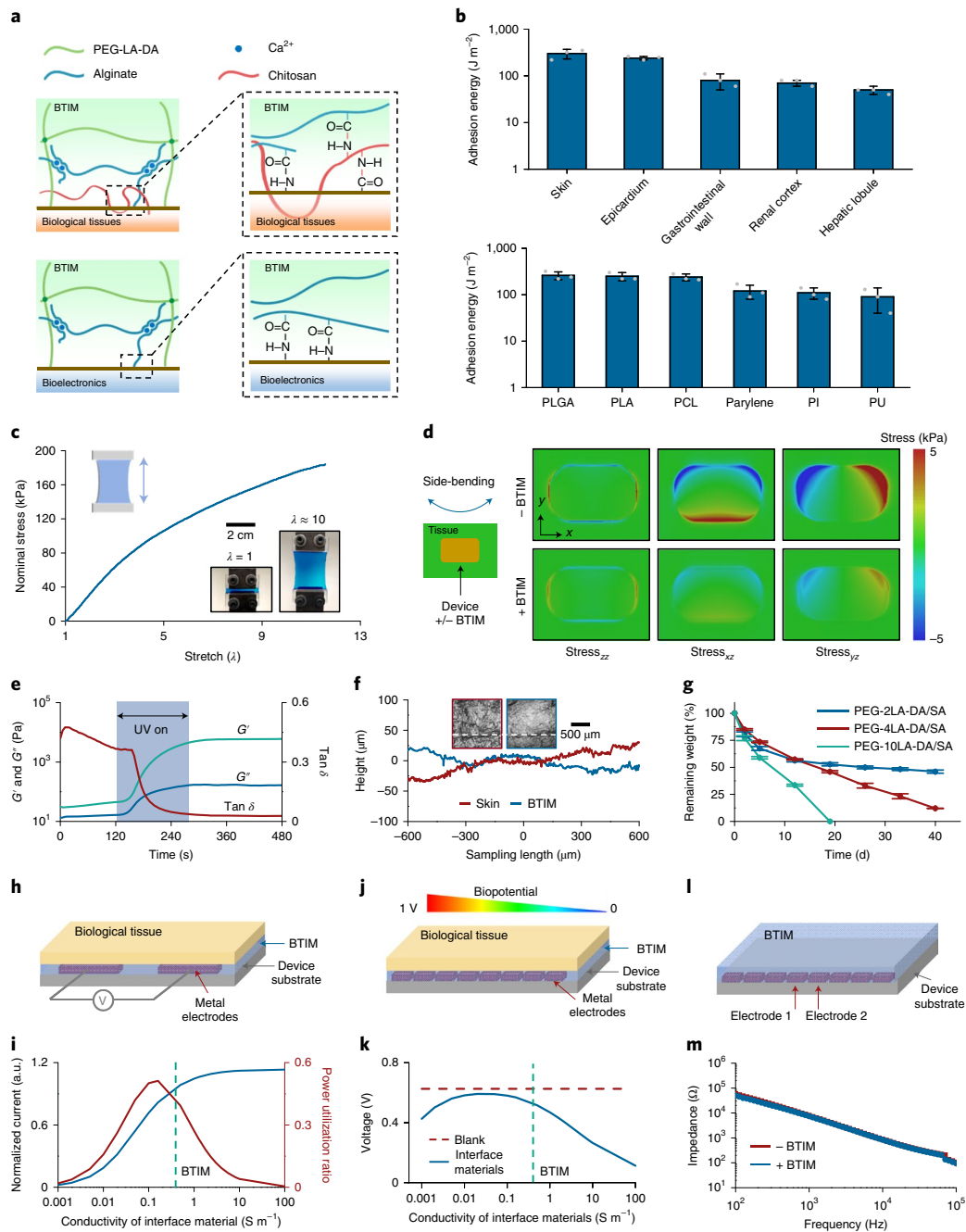


Fig. 2 | Key characteristics of the BTIM. **a, b**, Adhesion properties. **a**, Mechanisms of interfacial bonding to the surfaces of biological tissues (top) and bioelectronic devices (bottom). **b**, Adhesion energy between BTIM and a variety of tissues and device surfaces. PCL, polycaprolactone; PU, polyurethane. **c, d**, Mechanical properties. **c**, Stress–strain curves from samples of the BTIM. Inset: images of a BTIM specimen (coloured blue) before and after elongation without fracture. λ is defined as the ratio between the length during deformation and the initial length. **d**, Distribution of shear and normal stresses at the interface between a representative bioelectronic device (modulus 2 GPa) and underlying tissues (modulus 50 kPa) associated with side-bending (45°), determined by finite-element analysis. The layer of the BTIM (thickness 500 μm) decreases the maximum stresses by factors of 3.5, 3.3 and 3.3 for the zz , xz and yz components of the stress, respectively. **e, f**, Photoinitiated gelation. **e**, Photoinitiated transformation of viscous liquid precursors to elastic crosslinked solid adhesives occurs upon UV exposure for 180 s. **f**, Conformal coating of the BTIM on a piece of porcine skin resulting from this photoinitiated liquid-to-solid transformation. Surface height profiles of the porcine skin and the BTIM are along the white line in each corresponding 3D confocal optical microscopy image in the inset. **g**, Bioreabsorbability. Remaining weights of BTIM with PEG-2LA-DA/SA, PEG-4LA-DA/SA and PEG-10LA-DA/SA immersed in PBS (pH 7.4, 37°C) as a function of time. $n = 3$ independent samples in **b** and **g**. Values in **b** and **g** represent the mean \pm s.d. **h**, Schematic illustration of the working conditions for BTIM-assisted electrical stimulation. **i**, Calculated normalized current and power utilization ratio on the top surface of the myocardium layer as a function of the interface material conductivity. The values are normalized by those in the absence of the interface material. a.u., arbitrary units. **j**, Schematic illustration of the working conditions for BTIM-assisted biopotential mapping. **k**, Calculated potential on the electrode on the left-hand side in the presence of interface materials with various conductivities (blue) and in the absence of these materials (red). **l**, Schematic illustration of the experimental set-up to measure the impedance between two adjacent MEA electrodes. **m**, Representative impedance spectra of two adjacent MEA electrodes before (red) and after (blue) BTIM application in 0.1M PBS at room temperature.

3.5 relative to those without the BTIM. Increasing the thickness of the BTIM further decreases these stresses (Supplementary Fig. 10).

Photoinitiated transformation from viscous liquid-type precursors to an elastic crosslinked adhesives facilitates the formation of thin, conformal coatings directly on surfaces of interest. Figure 2e presents the rheological behaviour of the BTIM as a function of curing time. Free radical polymerization, initiated by ultraviolet (UV) exposure, yields a covalent network within 180 s (storage modulus, G' , from 30 to 6,000 Pa; $\tan \delta$ from 0.45 to 0.03, where δ is the phase angle between storage modulus and loss modulus). The initial storage modulus and viscosity ($\sim 2\text{--}3$ Pa s, similar to that of honey²⁶; detailed information in Supplementary Fig. 11) are associated with the rapid formation of the alginate ionic network upon application to tissue–electronics surfaces. The viscous characteristics prevent applied material from rapidly flowing away in an uncontrolled manner, to facilitate formation of spatially confined coatings with uniform thicknesses (detailed information in Supplementary Note 5). Applying and curing the BTIM in this fashion on porcine skin yields an interface that follows the natural texture of the tissue, as evidenced by inspecting the contacting surface following removal. Figure 2f presents surface height profiles of the porcine skin (arithmetic mean deviation of the roughness profile, R_a , 13.27 μm ; root mean squared of the roughness profile, R_{ms} , 16.88 μm) and the corresponding BTIM (R_a 9.60 μm ; R_{ms} , 10.98 μm) along the white line in each corresponding 3D confocal optical microscopic image in the inset and Supplementary Fig. 12. The strong correlation indicates that the liquid precursors wet and spread across rough tissue surfaces, thereby enhancing the adhesion strength by ensuring uniform contact. The photoinitiated gelation process also allows for casting onto highly structured and curved surfaces (detailed information in Supplementary Note 6). In fact, the precursors can completely fill the interior spaces of 3D bioelectronic systems without damaging fragile features, to achieve 3D electrode-embedded (Extended Data Fig. 1) and electrode-exposed (Supplementary Fig. 3) electronic structures.

The material is also bioresorbable through hydrolysis of lactide repeat units, aided by enzymatic reactions that can occur, as mediated by surrounding biofluids (Supplementary Note 7 and Supplementary Fig. 13). The lactide content determines the degradation lifetime, from ~ 20 d (PEG-10LA-DA system) to several months (PEG-2LA-DA system) in PBS (pH 7.4) at 37 °C in Fig. 2g. Such characteristics create opportunities for the use of the BTIM in bioresorbable electronic implants that support operation for a defined period of functional need and then disappear naturally²⁷. Furthermore, multiple experiments establish cytocompatibility and biocompatibility (Supplementary Figs. 14 and 15 and Supplementary Note 8).

The optical transparency and the ionic conductivity of the BTIM are additional essential features for functional optoelectronic and electronic interfaces. The transmittance of the samples (thickness 2 mm) is between 60 and 80% for wavelengths between 395 and 475 nm, and remains higher than 80% between 475 and 900 nm (Supplementary Fig. 16). The ionic conductivity is in the range of ~ 0.5 S m^{-1} at 1 kHz, similar to that of most biofluids. The BTIM can support bioelectronics for efficient local electrical stimulation and spatially resolved biopotential sensing. For electrical stimulation, a cardiac pacemaker serves as a representative example, shown in Fig. 2h. The normalized current in tissues and power consumption from Fig. 2i and Extended Data Fig. 3 suggest that the optimum conductivity for this scenario is 0.16–0.5 S m^{-1} , to avoid electrical connection block at low conductivity or electrical shorts at high conductivity. For biopotential sensing, a flexible MEA forms a representative example, shown in Fig. 2j. Figure 2k and Extended Data Fig. 4 present the measured potential at the electrode on the left-hand side as a function of conductivity, revealing that the optimum is 0.1–0.5 S m^{-1} . Such conductivities prevent signal

attenuation at low conductivity and shorts at high conductivity. Measurements with an ultrathin, flexible MEA (electrode dimensions 500 $\mu\text{m} \times 500 \mu\text{m}$; spacing 1 mm) demonstrate these principles (Fig. 2l and Supplementary Fig. 17). Representative impedance spectra between two adjacent MEA electrodes before (red) and after (blue) BTIM application (Fig. 2m) show negligible differences. Statistical results for impedance values before and after applying the BTIM in Supplementary Fig. 18 are 8.6 ± 0.3 k Ω and 8.2 ± 0.3 k Ω , respectively, at 1 kHz in 0.1 M PBS at room temperature. The results together prove that the BTIM layer can act as an attractive interfacial material for bioelectronics without substantial signal degradation. More generally, these studies also provide design guidelines for selecting the conductivity of an interface layer between bioelectronics devices and soft biological tissues. By using the proposed strategies, the need to pattern the interface materials is eliminated and gaps between tissues and electrodes can be avoided.

Wireless light delivery systems for optical stimulation

As an example of the use of the BTIM with an integrated device, Fig. 3a presents a wireless light delivery system (10 mm \times 6 mm \times 300 μm) with potential applications in phototherapy. This device consists of an inductive loop antenna, an inorganic light-emitting diode (ILED) and associated electronic components. The BTIM encapsulation coating (12 mm \times 8 mm \times 500 μm) secures the device to the dorsal subcutaneous area in a mouse model, as shown in Fig. 3b, with stable device operation during natural movements (Supplementary Video 1). Figure 3c demonstrates wireless activation of red (peak wavelength 630 nm) and green (peak wavelength 530 nm) ILEDs, selected for their relevance in tumour irradiation²⁸. The BTIM fixes the positions of implanted devices for several months. Evaluating the positions of encapsulated devices (totally 12 mm \times 8 mm \times 500 μm) by micro-computed tomography (MicroCT) along the diagonal (main), sagittal (first inset) and coronal (second inset) directions across days 2, 5 and 8 after surgery quantifies the positional stability, as shown in the first row of Fig. 3d. Within experimental uncertainties, the devices remain in their original locations throughout the period of study. Similar results are possible with the interface strategy (Supplementary Fig. 19a). By contrast, hydrogels (12 mm \times 8 mm \times 500 μm) with the same chemical formulations but applied without a primer fail to provide device/tissue adhesion and allow for obvious movements of the devices under otherwise identical conditions (second row in Fig. 3d). Two out of three of these devices emerged entirely from the body within 3 d after surgery through regions between the sutures. Analysis in Fig. 3e, Supplementary Fig. 19b, and Supplementary Note 9, indicates that the locations of devices integrated with the BTIM remain unchanged to within experimental uncertainties for up to 2 months, for both encapsulation and interface strategies (Fig. 3f and Supplementary Video 2). Furthermore, the devices remain functional throughout (Fig. 3g and Supplementary Video 3). By contrast, the displacements of the one device with a non-adhesive hydrogel that remained in the body of the animal are ~ 6 mm from day 2 to day 5 and ~ 17 mm from day 5 to day 8.

These materials and devices also present no measurable influence on the natural behaviours of the animals or their health status. Results of motion tracking (5 min in a rectangular arena) of mice implanted on day 10 and day 30 after surgery are similar to those of control animals without implants (Supplementary Fig. 20). The surgical wounds heal completely with regrown fur after several weeks (Fig. 3h and Supplementary Fig. 21). Histological analysis of the dorsal subcutaneous area of BTIM-implanted mice 4 weeks after surgery provides evidence of negligible influence on the morphology of the tissues and cells (Fig. 3i–k). Statistical analyses show that the adipocyte cell size, myofibre cell size and skin thickness are $1,030 \pm 150 \mu\text{m}^2$, $1,120 \pm 140 \mu\text{m}^2$ and $580 \pm 130 \mu\text{m}$,

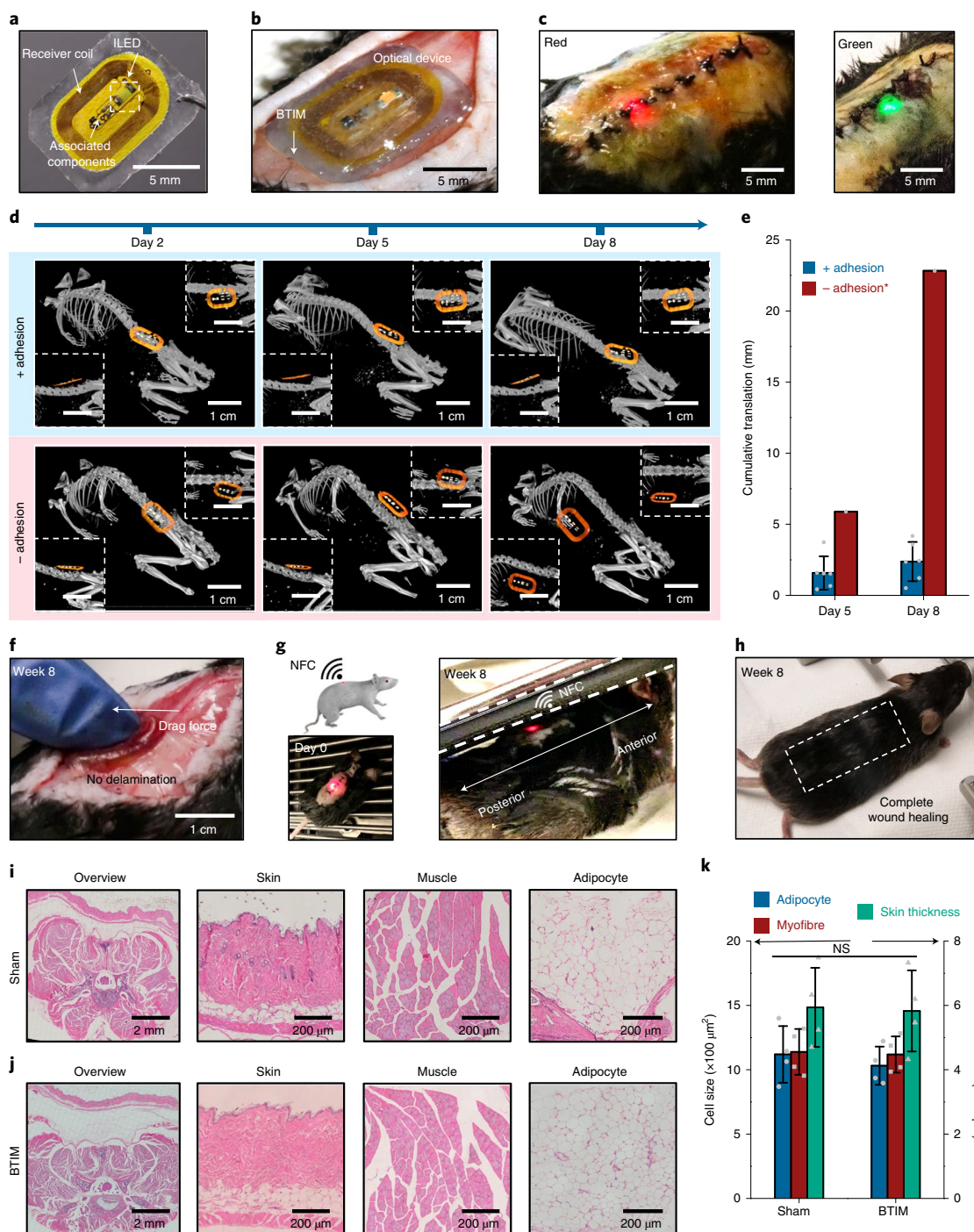


Fig. 3 | Soft adhesive interfaces between wireless optoelectronics and dorsal subcutaneous tissues. **a**, Image of a device (10 mm × 6 mm × 300 μm) that includes an inductive loop antenna, an ILED and associated electronic components. **b**, BTIM bonds the device to the dorsal subcutaneous area in a mouse model using the encapsulation strategy (adhesive size 12 mm × 8 mm × 500 μm; coloured blue). **c**, Wireless activation of red (peak wavelength 630 nm) and green (peak wavelength 530 nm) ILEDs, selected for their relevance in tumour irradiation in dorsal subdermal tissues. **d**, Positions of encapsulated devices along the diagonal (main), sagittal (first inset) and coronal (second inset) directions on days 2, 5 and 8 after surgery as determined by MicroCT. Hydrogels with the same chemical formulations but without the use of a primer serve as the control group. **e**, Statistical analysis of the displacements of devices encapsulated using the BTIM with primer (blue) and without (red). *Two of the three devices in the second case exited the animal within 3 d after surgery. **f**, Image illustrating robust adhesion 2 months after surgery in a manual stress test. **g**, Schematic illustration and image of wireless light activation in a chamber based on near-field communication (NFC) technology immediately after surgery (left) and 2 months after surgery (right). **h**, Image of complete wound healing of the surgical site after several weeks with fur regrown. **i, j**, Haematoxylin and eosin stains of the dorsal overview, skin, muscle and adipocyte in sham (**i**) and BTIM (**j**) groups 1 month after surgery. **k**, Statistical analyses of the adipocyte cell size, myofibre cell size and skin thickness in both groups. Neither the cell sizes nor the skin thicknesses present significant differences between sham and BTIM groups ($P=0.5324$ for adipocyte cell size, $P=0.8650$ for myofibre cell size and $P=0.9035$ for skin thickness). $n=6$ biologically independent animals for “+ adhesion” group and $n=3$ biologically independent animals for “- adhesion” group in **a–h**, and $n=4$ biologically independent animals in **i–k**. Values in **e** and **k** represent the mean \pm s.d. Statistical significance and P values are determined by two-sided Student’s t -test at a significance level of 0.05. NS indicates no statistically significant differences.

respectively, in the BTIM group. These values in the sham group are $1,120 \pm 220 \mu\text{m}^2$, $1,140 \pm 180 \mu\text{m}^2$ and $590 \pm 120 \mu\text{m}^2$, respectively.

Wireless optogenetic electronic platforms

Similar adhesive strategies are effective for devices that support optogenetic stimulation^{21,29–31} in the deep brain. Figure 4a shows a lightweight, thin, battery-free and wireless device for this application. This system includes a filamentary probe that supports a microscale ILED (μ -ILED; wavelength 590 nm) at its tip end for insertion into a targeted region of the brain. The back end consists of a receiver coil that supports wireless inductive power harvesting, along with associated interconnects and components. This part of the system mounts on the skull firmly with the BTIM using the encapsulating strategy (detailed surgical procedures in Supplementary Fig. 22). Figure 4b and Supplementary Videos 4 and 5 highlight the stable positioning of the receiver coils and interconnects using the BTIM (thickness 300 μm). Figure 4c shows a combined image that overlays magnetic resonance imaging (MRI) slices with MicroCT reconstructions 2 weeks after surgery, to highlight the positions of the device and the BTIM. The devices enable deep tissue optogenetic stimulation with lifetimes of at least 2 weeks (insets of Fig. 4c and Supplementary Video 6). Furthermore, for transcranial optogenetic experiments, similar evaluations of the device positions by MicroCT prove that the BTIM-encapsulated device remains in its original location throughout the period of study, to within experimental uncertainties (Fig. 4d, Supplementary Note 9 and Extended Data Fig. 5), unlike non-adhesive devices. Stabilization of the μ -ILED provided by BTIM greatly increases the rate of success in such experiments.

Immunostaining of glial cell markers (glial fibrillary acidic protein, GFAP; ionized calcium binding adaptor molecule 1, IBA1) determines the activation of astrocytes and microglial cells in response to BTIM (thickness $\sim 500 \mu\text{m}$) and sham surgery (Fig. 4e,f and Extended Data Fig. 6a–c). For GFAP, the astrocyte area percentages are $22 \pm 4\%$ for the sham group and $25 \pm 3\%$ for the BTIM group. For IBA1, the microglia area percentages are $14 \pm 8\%$ for the sham group and $13 \pm 3\%$ for the BTIM group. The negligible difference is evidence for the biocompatibility of the BTIM with brain tissue. Furthermore, the results clearly have potential for use in mice genetically modified for optogenetic studies, with robust adhesion to the cerebrum (Extended Data Fig. 6d,e and Supplementary Video 7).

Bioresorbable optical filters

The BTIM can also be used to secure bioresorbable optical filters³² on the exposed surface of the brain for at least 2 weeks (Fig. 4g,h and Supplementary Fig. 23), providing a potential means for spectroscopic characterization of physiological status and neural activity³². The filter (Supplementary Fig. 24) examined here consists of 15 pairs of SiO_x and SiN_y layers (thicknesses 54 and 85 nm, respectively) on a film of PLGA (thickness 10 μm). The transmission spectrum reveals that the device encapsulated with the BTIM can effectively block excitation light (wavelength 450–520 nm) and transmit emission light (wavelength 520–900 nm), as shown in Fig. 4i. This transmission window is relevant to applications that characterize neural calcium transients using genetically encoded fluorescent calcium indicators^{32–35}.

Interconnects/cables with adhesive conduits

Other classes of devices include wireless bioelectronic systems with sensors or actuators that lie in deep tissues at locations of interest^{30,36}. In such cases, interconnects/cables often span between these components and functional modules that reside in subcutaneous tissues, typically for power harvesting, wireless communication and/or analogue–digital conversion. The schematic illustration in Fig. 4j shows how the encapsulation strategy can yield an adhesive

tunnel, or conduit, in a soft, deformable encapsulation structure of BTIM that bonds to the surrounding tissues but not to the enclosed interconnects/cables. The interconnect/cable surfaces exclude the (3-aminopropyl)triethoxysilane (APTES) functionalization. Such approaches effectively confine the motion of the interconnects/cables to eliminate adverse effects on the system and the adjacent tissues. The result allows for flexible and reliable electrical connections under a variety of working conditions (Fig. 4k,l and Supplementary Video 8).

Wireless electrical cardiac pacing

Stable electrical interfaces for measurements and stimulation are essential in many biological applications, especially for the cardiac system. The inset in Fig. 5a highlights a thin, flexible, miniaturized, battery-free, wireless, leadless cardiac pacemaker (40 mm \times 10 mm \times 200 μm) that includes a pair of pacing electrodes, along with a rectangular PLGA/polyurethane frame (8 mm \times 8 mm; detailed information in Supplementary Fig. 25), designed to attach to the anterior epicardial surface of the ventricles. The BTIM coating establishes conformal contact between the electrodes and the myocardium, as shown in Fig. 5a and Supplementary Video 9. This scheme yields a gentle, conductive, stable interface between the device and the beating heart (Fig. 5b, left; detailed surgical procedures in Supplementary Fig. 26a–f), without tissue damage or bleeding during suturing (Fig. 5b, right). Composite images (Fig. 5c, top) highlight attachment of the electrodes to the heart 1 week after surgery. The magnified image in Fig. 5c (bottom) shows the position within the rat anatomy. Manual mechanical tests indicate strong adhesion (Fig. 5d, Supplementary Fig. 26g–i and Supplementary Videos 10 and 11) for 10 d after surgery.

Histological evaluations of fibrotic tissues as in Fig. 5e serve as a basis for comparing pacemakers secured with sutures (top) and those with the BTIM (bottom). Although the levels of fibrosis in the two cases are similar, large perforations in the cardiac muscle appear with surrounding fibrotic tissues induced by the suturing process, potentially resulting in compromised mechanical contraction of the myocardium and in life-threatening arrhythmias during implantation procedures and after surgery. The differences are evident in a double-blinded clinical-scoring system highlighted in Fig. 5f, which defines the amount of disorganized connective tissue on top of the myocardium on a scale of 0–5. The clinical score for suturing is 2.8 ± 0.3 ($P=0.0215$ versus control group), consistent with dense scar tissue that requires sharp instrumentation to disrupt. The score for the BTIM is 1.8 ± 0.6 ($P=0.4334$ versus control group), corresponding to a relatively small amount of scar tissue that can be disrupted with blunt instruments. As shown in Fig. 5g, Masson's trichrome staining of tissue cross-section 4 weeks after surgery indicates volume fractions of interstitial space, myocytes and collagenous tissue, which are $10 \pm 6\%$, $69 \pm 12\%$ and $21 \pm 9\%$, respectively. For the case of sutures, these same quantities are $10 \pm 5\%$, $78 \pm 7\%$ and $12 \pm 7\%$ and in the control group $6 \pm 4\%$, $85 \pm 7\%$ and $9 \pm 4\%$. Compared with the control group, the BTIM induces no significant differences in myocardial volume fraction, which is consistent with an absence of myocardial damage.

Differences in biocompatibility at the electrode–tissue interface are largely responsible for differences between functional lifetimes of pacemakers implanted with the BTIM and with sutures. Studies to compare these two options involve daily pacing trials under light sedation with electrocardiogram (ECG) recordings (Supplementary Note 10 and Supplementary Fig. 27). Figure 5h compares the threshold voltages for pacing. Values for the sutured devices increase rapidly and reach a failure criterion (0.7 V) on day 6 after surgery (one of the two devices failed to pace within 1 d). Failure results are mainly due to an increased level of disorganized non-conductive connective tissue that develops at the surface of the myocardium, as evaluated by the clinical score in Fig. 5f. By comparison, devices mounted with the BTIM allow pacing up to day 8 after surgery, with

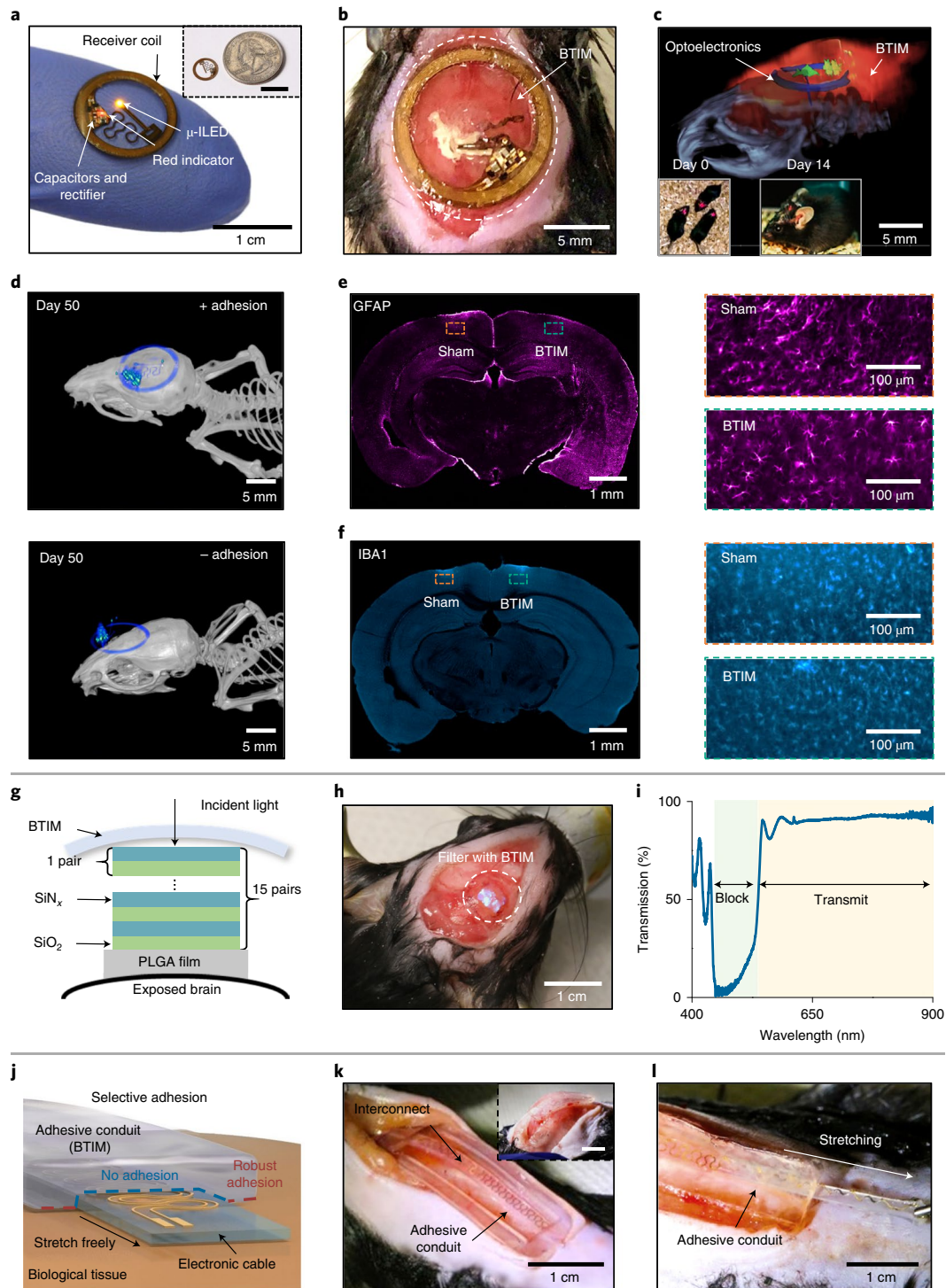


Fig. 4 | Securing optical devices onto the brain and forming adhesive conduits for interconnects. a–f, Wireless optogenetic devices. **a,** Image of a thin, battery-free wireless device that includes a filamentary probe with a μ -ILED (wavelength 590 nm) Inset: image of a device placed near a quarter. **b,** Stable positioning of the receiver coil and interconnects secured by the BTIM. **c,** Visualization of implanted devices through a combined image that overlays MRI slices with MicroCT reconstructions 2 weeks after surgery. Insets: deep-tissue optogenetic stimulation immediately after surgical implantation (left) and 14 d after surgery (right). **d,** MicroCT images of the BTIM-encapsulated (top) and non-adhesive (bottom) devices on the skull for transcranial optical stimulation on day 50 after surgery. **e, f,** GFAP (**e**; coloured magenta) and IBA1 (**f**; coloured cyan) staining on the cerebrum directly exposed to the BTIM and the cerebrum sham (orange inset, sham group; blue inset, BTIM group). $n = 3$ biologically independent animals in **a–d** and $n = 4$ biologically independent animals in **e–f**. **g–i,** Bioresorbable optical filters. **g,** Cross-sectional illustration of a bioresorbable optical filter secured on an exposed region of the brain by the BTIM. **h,** Images to illustrate stable positioning of the filter by use of the BTIM with the encapsulation strategy. **i,** Transmission spectrum of a BTIM-encapsulated, bioresorbable optical filter. **j–l,** Adhesive conduits for interconnects/cables. **j,** Schematic illustrations of an adhesive tunnel, or conduit, that anchors the interconnects/cables onto tissues but allows their free motion within it. **k, l,** Images that illustrate stable positioning of an interconnect/cable by an adhesive conduit. The adhesive conduit allows for the interconnect/cable to be bent (inset in **k**) and stretched during normal use (**l**).

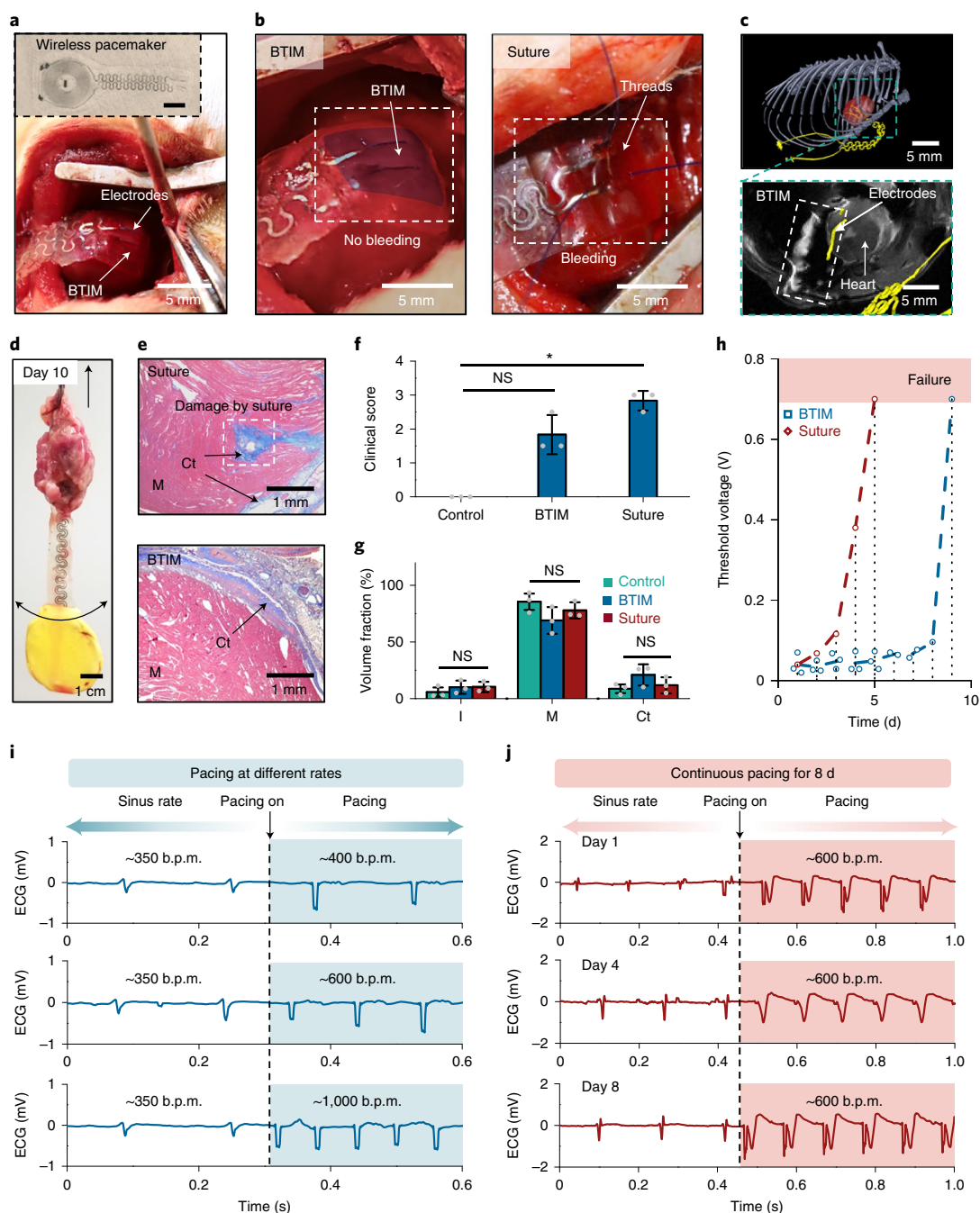


Fig. 5 | Soft adhesive interfaces between wireless cardiac pacemakers and the myocardium. a, Image of the pacemaker and the process of adhering the electrodes to the myocardium in a rat model using the encapsulation strategy. Inset: thin, flexible wireless cardiac pacemaker that includes a radiofrequency power harvester positioned in the lateral dorsal subcutaneous pocket, with a pair of pacing electrodes that attaches onto the anterior epicardial surface of the ventricles. **b**, Gentle, conductive, stable interface formed by the BTIM (left; coloured blue) avoids tissue damage and bleeding, which typically occurs with suturing (right). **c**, Positions of the electrodes and the BTIM illustrated with an overlay of MRI with MicroCT images 1 week after surgery. **d**, Manual mechanical tests demonstrate the strength of adhesion on day 10 after surgery. **e**, Representative images of Masson's trichrome stained cross-sections compare implants secured with sutures (top) and the BTIM (bottom). M, myocytes; Ct, collagenous tissue. **f**, More disorganized connective tissue on top of the myocardium for pacemakers secured with sutures compared to the BTIM group at 4 weeks post-implantation. Kruskal-Wallis test, $H(2) = 7.245$, $P = 0.0071$; post hoc Dunn multiple-comparison test, $P_{(\text{control vs BTIM})} = 0.4334$, $*P_{(\text{control vs suture})} = 0.0215$. **g**, Masson's trichrome staining of the epicardium near the site of pacemaker attachment 4 weeks after surgery for suture and BTIM methods quantifies negligible changes in the volume fractions of interstitial space (I), myocardium and fibrosis in cardiac cross-sections. Kruskal-Wallis test, $H(2) = 0.6222$, $P = 0.8286$. Post hoc Dunn multiple-comparison test, $P > 0.9999$. $n = 3$ biologically independent animals in **a-g**. Values in **f,g** represent mean \pm s.d. Statistical significance and P values are determined by Kruskal-Wallis test and post hoc Dunn multiple-comparison test at a significance level of 0.05. NS indicates no statistically significant differences; $*P \leq 0.05$ is considered statistically significant. **h**, Threshold voltages for pacing to compare pacemakers secured with sutures and the BTIM. (One of the two sutured pacemakers failed to pace on day 1 after surgery; dashed lines indicate the average values on each day; dotted lines indicate the operating day). **i**, Representative ECG recordings show conversion from normal sinus rhythm to pacing rates of ~400, 600 and 1,000 b.p.m., respectively. **j**, Representative ECG recordings on days 1, 4 and 8 after implantation.

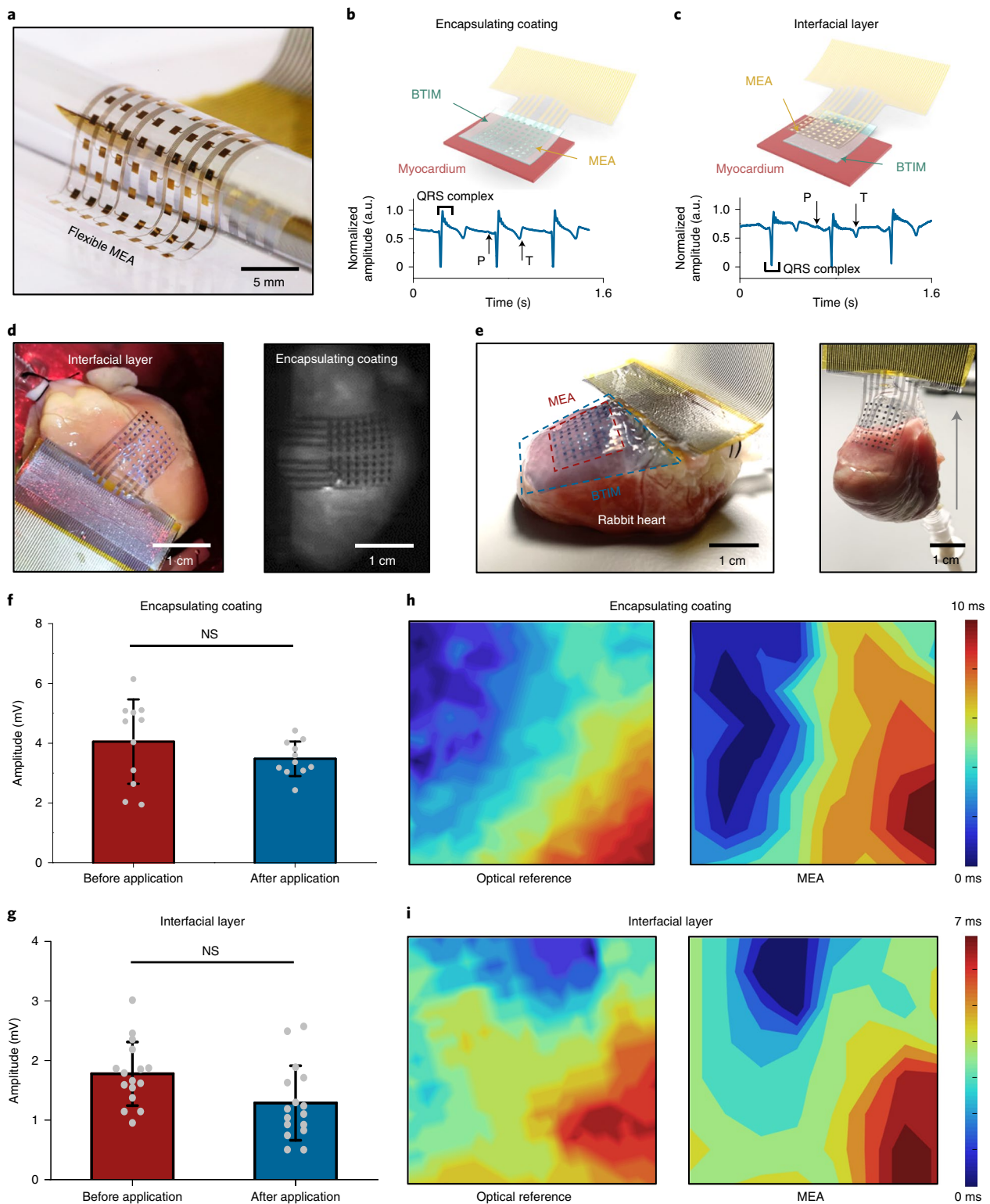


Fig. 6 | Ultrathin, flexible MEAs adhered to the epicardium. **a**, Image of an MEA device designed for spatiotemporal mapping with 64 electrodes (eight columns, eight rows). **b,c**, Top: schematic illustrations of integration strategies based on the encapsulation (**b**) and the interface (**c**) schemes. Bottom: high-quality normalized electrograms of sinus rhythms from a representative electrode in devices adhered using each of these methods. **d**, MEA configuration on the epicardial surface for both methods (encapsulating coating and interfacial layer). **e**, Left: positioning of the heart, the electrode array and the BTIM (coloured blue). Right: stable adhesion after 8 h of testing in the Langendorff perfusion system. **f,g**, Amplitudes of electrograms recorded with devices after integration with the encapsulation (**f**) and interface (**g**) methods. The results are similar to those collected with devices held by capillary interaction ($P=0.5195$ for encapsulating coatings and $P=0.0507$ for interface layers). $n=11$ independent electrodes in **f** and $n=16$ independent electrodes in **g**. Values in **f** and **g** represent the mean \pm s.d. Statistical significance and P values are determined using a Wilcoxon matched-pairs signed-rank test at a significance level of 0.05. NS indicates no statistically significant differences. **h,i**, Strong spatial correlations of time-coincident optical (left) and electrical activation maps (right) recorded with MEAs attached by the encapsulation (**h**) and interface (**i**) methods.

only slight increases in threshold voltage (0.04 V on day 1; 0.10 V on day 8). Figure 5i presents representative ECG traces recorded during rapid ventricular pacing in different rhythms on day 0, at ~400, 600 and 1,000 beats per minute (b.p.m.) (Supplementary Video 12). Figure 5j similarly shows ECG traces obtained throughout the pacing period of 8 d after surgery, with a minimal increase in threshold voltage (full pacing details shown in Supplementary Fig. 28).

Electrical spatiotemporal mapping

The same adhesive strategy can be used for mapping of cardiac electrophysiology using flexible electrode arrays, without the limitations associated with previously described schemes^{37,38}. Figure 6a presents a device designed for this purpose with 64 electrodes (MEA; eight columns, eight rows; parylene/Cr/Au/parylene: 4/0.01/0.3/4 µm; 500 µm × 500 µm for each electrode; 13 mm × 13 mm in total). Figure 6b,c provides schematic illustrations and images of integration strategies based on the BTIM encapsulation (Fig. 6b) and interface (Fig. 6c) methods (thickness 500 µm) on Langendorff-perfused rabbit hearts in a constant-pressure system *ex vivo*. High-quality normalized electrograms of sinus rhythms from a representative electrode associated with these methods verify the ability to capture electrophysiological signals (ECG traces measured from each electrode appear in Supplementary Fig. 29). Images in Fig. 6d show the MEA configuration on the epicardial surface (left, interfacial layer; right, encapsulating coating). The photographs in Fig. 6e highlight stable adhesion after 8 h of testing in the Langendorff perfusion system, including manual evaluations of the robustness of the bonding. The adhesion strength supports gravitational forces associated with the rabbit heart (weight ~8 g) with negligible delamination.

The amplitudes of electrograms recorded with devices after integration with these methods, as shown in Fig. 6f,g, are similar to those collected with devices held by capillary forces associated with the presence of biofluids. Specifically, data collected before and after applying the encapsulation method are 4.1 ± 1.4 mV and 3.5 ± 0.6 mV, respectively; those with the interfacial method are 1.8 ± 0.5 mV and 1.3 ± 0.6 mV, respectively. The time coincidence of simultaneous recordings of electrograms and optical action potentials indicates consistency between these two signals, showing the effectiveness of the BTIM for cardiac mapping applications (Supplementary Fig. 30). Strong spatial correlations of time-coincident optical (left; captured at 100 pixels × 100 pixels) and electrical activation maps (right; captured with 8 × 8 electrode array; lineshape fitting) recorded with MEAs attached by the encapsulation (Fig. 6h) and interface (Fig. 6i) methods provide further evidence of proper operation of MEAs with the BTIM. Such an integrated system can also accurately map ventricular fibrillation, as shown in Extended Data Fig. 7 and Supplementary Video 13.

Conclusions and outlook

The results described here span topics in material formulations, integration schemes and *in vivo* evaluations of functional, soft adhesive materials for bioelectronic–tissue interfaces. Systematic studies of the chemical, mechanical, electrical and optical properties define the key materials science aspects of this system. Comprehensive evaluations in animal models illustrate all of the essential features as well as its applicability to a diverse collection of bioelectronics devices across multiple organs. In all cases, the BTIM softly joins these electronic/optoelectronic devices to moving tissues as functional interfaces for sensing and stimulation, without adverse immune responses or device dislocation. These materials strategies have immediate potential for applications in biological research on animal models, and they offer promise for eventual use in humans. The concepts may also form a starting point for further developments of advanced biotic–abiotic interfaces to support multifunctional diagnosis and treatment in both acute and chronic medical applications. Additional improvements in interfacial chemistry may

allow for robust stable bonding between bioelectronics systems and tissue surfaces throughout the course of chronic diseases and disorders, where the timescales may extend from many months to years (discussions on potential failure modes and solutions to long-term material and device reliability appear in Supplementary Note 11). Other possibilities lie in the development of materials that support the bidirectional transport of drugs or biochemical species, to complement capabilities provided by electrical and/or optical interfaces.

Online content

Any methods, additional references, Nature Research reporting summaries, source data, extended data, supplementary information, acknowledgements, peer review information; details of author contributions and competing interests; and statements of data and code availability are available at <https://doi.org/10.1038/s41563-021-01051-x>.

Received: 11 June 2020; Accepted: 11 June 2021;

Published online: 29 July 2021

References

- Kalantar-Zadeh, K. et al. A human pilot trial of ingestible electronic capsules capable of sensing different gases in the gut. *Nat. Electron.* **1**, 79–87 (2018).
- Dagdeviren, C. et al. Flexible piezoelectric devices for gastrointestinal motility sensing. *Nat. Biomed. Eng.* **1**, 807–817 (2017).
- Feiner, R. et al. Engineered hybrid cardiac patches with multifunctional electronics for online monitoring and regulation of tissue function. *Nat. Mater.* **15**, 679–685 (2016).
- Jun, J. J. et al. Fully integrated silicon probes for high-density recording of neural activity. *Nature* **551**, 232–236 (2017).
- Mickle, A. D. et al. A wireless closed-loop system for optogenetic peripheral neuromodulation. *Nature* **565**, 361–365 (2019).
- Feiner, R. & Dvir, T. Tissue–electronics interfaces: from implantable devices to engineered tissues. *Nat. Rev. Mater.* **3**, 17076 (2018).
- Yang, C. & Suo, Z. Hydrogel ionotronics. *Nat. Rev. Mater.* **3**, 125–142 (2018).
- Yuk, H., Lu, B. & Zhao, X. Hydrogel bioelectronics. *Chem. Soc. Rev.* **48**, 1642–1667 (2019).
- Wound Closure Products Market By Product type Analysis (Sutures, Adhesives and Tissue Sealants, Hemostats, Surgical Staples, Wound Closure Strips) and By Regional Analysis – Global Forecast by 2021–2026*. Report MDWCM417 (Market Research Engine, 2019); <https://www.marketresearchengine.com/wound-closure-products-market>
- Potvin, R., Matossian, C. & Makari, S. Cataract surgery and methods of wound closure: a review. *Clin. Ophthalmol.* **2015**(9), 921–928 (2015).
- Edmiston, C. E. et al. Microbiology of explanted suture segments from infected and noninfected surgical patients. *J. Clin. Microbiol.* **51**, 417–421 (2013).
- Owens, C. D. & Stoessel, K. Surgical site infections: epidemiology, microbiology and prevention. *J. Hospital Infect.* **70**, 3–10 (2008).
- Mond, H. G., Helland, J. R., Stokes, K., Bornzin, G. A. & McVenes, R. The electrode–tissue interface: the revolutionary role of steroid-elution. *Pacing Clin. Electrophysiol.* **37**, 1232–1249 (2014).
- Yuk, H. et al. Dry double-sided tape for adhesion of wet tissues and devices. *Nature* **575**, 169–174 (2019).
- Li, J. et al. Tough adhesives for diverse wet surfaces. *Science* **357**, 378–381 (2017).
- Lin, X. et al. A viscoelastic adhesive epicardial patch for treating myocardial infarction. *Nat. Biomed. Eng.* **3**, 632–643 (2019).
- Liang, S. et al. Paintable and rapidly bondable conductive hydrogels as therapeutic cardiac patches. *Adv. Mater.* **30**, 1704235 (2018).
- Gan, D. et al. Plant-inspired adhesive and tough hydrogel based on Ag–lignin nanoparticles-triggered dynamic redox catechol chemistry. *Nat. Commun.* **10**, 1487 (2019).
- Blacklow, S. O. et al. Bioinspired mechanically active adhesive dressings to accelerate wound closure. *Sci. Adv.* **5**, eaaw3963 (2019).
- Wang, X. et al. Three-dimensional electronic scaffolds for monitoring and regulation of multifunctional hybrid tissues. *Extreme Mech. Lett.* **35**, 100634 (2020).
- Shin, G. et al. Flexible near-field wireless optoelectronics as subdermal implants for broad applications in optogenetics. *Neuron* **93**, 509–521.e3 (2017).
- Koo, J. et al. Wireless bioresorbable electronic system enables sustained nonpharmacological neuroregenerative therapy. *Nat. Med.* **24**, 1830–1836 (2018).
- Yu, K. J. et al. Bioresorbable silicon electronics for transient spatiotemporal mapping of electrical activity from the cerebral cortex. *Nat. Mater.* **15**, 782–791 (2016).

24. Mathur, A. B., Collinworth, A. M., Reichert, W. M., Kraus, W. E. & Truskey, G. A. Endothelial, cardiac muscle and skeletal muscle exhibit different viscous and elastic properties as determined by atomic force microscopy. *J. Biomech.* **34**, 1545–1553 (2001).
25. Arda, K., Ciledag, N., Aktas, E., Aribas, B. K. & Köse, K. Quantitative assessment of normal soft-tissue elasticity using shear-wave ultrasound elastography. *Am. J. Roentgenol.* **197**, 532–536 (2011).
26. Yanniotis, S., Skaltsi, S. & Karaburnioti, S. Effect of moisture content on the viscosity of honey at different temperatures. *J. Food Eng.* **72**, 372–377 (2006).
27. Kang, S.-K. et al. Bioresorbable silicon electronic sensors for the brain. *Nature* **530**, 71–76 (2016).
28. Yamagishi, K. et al. Tissue-adhesive wirelessly powered optoelectronic device for metronomic photodynamic cancer therapy. *Nat. Biomed. Eng.* **3**, 27–36 (2019).
29. Zhang, Y. et al. Battery-free, lightweight, injectable microsystem for in vivo wireless pharmacology and optogenetics. *Proc. Natl Acad. Sci. USA* **116**, 21427–21437 (2019).
30. Gutruf, P. et al. Fully implantable optoelectronic systems for battery-free, multimodal operation in neuroscience research. *Nat. Electron.* **1**, 652–660 (2018).
31. Burton, A. et al. Wireless, battery-free subdermally implantable photometry systems for chronic recording of neural dynamics. *Proc. Natl Acad. Sci. USA* **117**, 2835–2845 (2020).
32. Bai, W. et al. Bioresorbable photonic devices for the spectroscopic characterization of physiological status and neural activity. *Nat. Biomed. Eng.* **3**, 644–654 (2019).
33. Tharanathan, R. N. Biodegradable films and composite coatings: past, present and future. *Trends Food Sci. Technol.* **14**, 71–78 (2003).
34. Boutry, C. M. et al. Towards biodegradable wireless implants. *Phil. Trans. R. Soc. A* **370**, 2418–2432 (2012).
35. Chen, T.-W. et al. Ultrasensitive fluorescent proteins for imaging neuronal activity. *Nature* **499**, 295–300 (2013).
36. Yang, Y. et al. Wireless multilateral devices for optogenetic studies of individual and social behaviors. *Nat. Neurosci.* **24**, 1035–1045 (2021).
37. Fang, H. et al. Capacitively coupled arrays of multiplexed flexible silicon transistors for long-term cardiac electrophysiology. *Nat. Biomed. Eng.* **1**, 0038 (2017).
38. Lee, W. et al. Nonthrombogenic, stretchable, active multielectrode array for electroanatomical mapping. *Sci. Adv.* **4**, eaau2426 (2018).

Publisher's note Springer Nature remains neutral with regard to jurisdictional claims in published maps and institutional affiliations.

© The Author(s), under exclusive licence to Springer Nature Limited 2021

Methods

Materials. The starting materials included polyethylene glycol (weight-averaged molecular mass, M_w , 35 kDa), 2-hydroxy-1-[4-(2-hydroxyethoxy) phenyl]-2-methyl-1-propanone (Irgacure D-2959), lactide, triethylamine, acryloyl chloride, tin(II) 2-ethylhexanoate (Sn(Oct)₂), dichloromethane (anhydrous), toluene (anhydrous), potassium carbonate (K₂CO₃), calcium chloride (CaCl₂) and magnesium sulfate (MgSO₄) purchased from Sigma-Aldrich, ethyl ether (anhydrous) purchased from Thermo Fisher Scientific, microfiltered and lyophilized SA (MVG GRGDSP coupled; high G ratio; high M_w) purchased from NovaMatrix (Dupont), high-purity chitosan (99% degree of deacetylation; M_w 100 kDa), as primers for tissues, purchased from Sigma-Aldrich, and EDC and Sulfo-NHS, as coupling reagents for tissue and device primers, purchased from Thermo Fisher Scientific. The solvents included ultrapure distilled water, PBS (pH 7.4) and MES (pH 5.0) purchased from Thermo Fisher Scientific. All chemicals were used as received. Tissues and organs for bench studies were purchased from Animal Biotech Industries and were cleaned with soap and water before adhesion measurements.

Synthesis. Synthesis of polyethylene glycol-lactide (PEG-LA) bioresorbable copolymer. The α - and ω -hydroxyl end groups of commercial PEG served as ring-opening reagents to initiate the polymerization of lactide to form copolymers. The number of lactide units, defined by x ($x = 2, 4$ and 10) in PEG- x LA, determines the degradation rate of the material, where x refers to the theoretical number-averaged degree of polymerization of lactide on each end of the PEG. Dissolving PEG (1 equivalent (eq.), 54 g) in 170 ml anhydrous toluene mixed with lactide (2 eq., 0.358 g) and Sn(Oct)₂ (0.1 eq., 0.062 g), followed by purging with nitrogen and then heating at 110 °C for 24 h under constant stirring, formed the PEG-2LA. Precipitating the PEG-2LA in anhydrous ethyl ether, followed by filtering and drying under vacuum for 24 h at room temperature, yielded dry PEG-2LA with hydroxyl end groups. Adding different amounts of lactide monomers during the reaction formed corresponding PEG-4LA and PEG-10LA terminated with hydroxyl groups.

Synthesis of PEG- x LA-DA macromer. The addition of acrylate end groups to hydroxyl-terminated PEG- x LA yielded polymerizable macromers, via the following steps³⁹. PEG- x LA (1 eq., 50 g) and triethylamine (4 eq., 0.83 ml) were dissolved in 500 ml anhydrous dichloromethane and then cooled to 0 °C in an ice bath. Acryloyl chloride (4 eq., 0.5 ml) was added dropwise under constant stirring, followed by reaction for 12 h at 0 °C and 12 h at room temperature, respectively. The PEG- x LA-DA solution was washed with 5 wt% K₂CO₃ solution, dried with MgSO₄ and precipitated in ethyl ether. Further purification of PEG- x LA-DA involved two cycles of dissolution and precipitation in dichloromethane and ethyl ether, respectively. Drying under vacuum conditions for 24 h at room temperature completed the synthesis of the polymerizable macromers. The materials were characterized using an AVANCE III-500 MHz solution NMR spectrometer with a DCH cryoprobe (Bruker) and MALDI-ToF (matrix-assisted laser desorption/ionization-time of flight; Bruker). ¹H NMR data were collected using a TopSpin 3.6.2 (Bruker) and analysed using Mnova 8.1.4 (Bruker). Mass spectra were collected using flexAnalysis 3.4 (Bruker) and PolyTools 2.0 (Bruker).

Synthesis of the BTIM. Synthesis began with dissolving PEG-LA-DA (40.0 wt%), Irgacure D-2959 (0.4 wt%) and CaCl₂ (0.5 wt%) in ultrapure water to form solution A (pH 7). Dissolving SA (5.0 wt%) in ultrapure water formed solution B (pH 7). Bubbling N₂ into solutions A and B for 10 min followed by degassing removed most of the dissolved O₂. Mixing solutions A and B at a ratio of 1:1 followed by exposure under UV light (wavelength 365 nm; density 20 mW cm⁻²) for 3 min cured the bioadhesives, in a standard process used throughout the experiments and studies presented here.

The primers utilized carbodiimide reagents (EDC, 0.5 wt%; Sulfo-NHS, 0.5 wt%) in MES buffer (pH 5). Certain steps in the synthesis followed protocols published in a previous study¹⁵. The process began with dissolving chitosan (2.0 wt%) in MES buffer (pH 5) followed by the addition of carbodiimide reagents (EDC, 0.5 wt%; Sulfo-NHS, 0.5 wt%).

Integration strategies. Encapsulating coating. The procedure began with placing the device on the tissue and then spreading primers on the surfaces of both. Introducing a mixture of solutions A and B onto the device and adjacent areas of tissue and then exposing to UV completed the process.

Interfacial layer. The procedure began with treating the bottom surface of the device with UV-induced ozone to create surface hydroxyl groups, followed by soaking in APTES (5 vol% in a mixture of ethanol and water at a ratio of 1:1) for 30 min to form amine termination. After APTES functionalization (detailed information in Supplementary Note 3), the device surfaces were immediately rinsed using ethanol, isopropyl alcohol and DI water in sequence, each for 2 min, followed by immersion in DI water for 5 min, to remove the residues of ethanol and APTES. Functionalization was assessed through ToF secondary-ion mass spectrometry analysis and measurement of APTES thickness through spectroscopic ellipsometry utilized WinCadence 5.4.0.5 (Physical Electronics)

and EASE 3.01D (J.A. Woollam), respectively. Applying primers and precursor mixtures, sequentially, at the interface between the tissue and the device, followed by UV exposure, formed a strongly bonded interface. For opaque devices, adding transparent materials, such as PLGA or parylene, around the perimeter (extending length ~2 mm) yielded sites for interfacial bonding.

Supporting matrix. The techniques of compressive buckling formed the 3D electronic structures presented⁴⁰ here. The strategy began with casting the precursor mixture onto the structures, followed by UV exposure, to yield a free-standing component with BTIM as a matrix supporting the 3D electronic structure inside. Applying primers and additional precursor mixtures to the surfaces of this system and the tissue, followed by manual placement and UV curing, completed the integration.

Characterization of the BTIM. Adhesion energy. Characterization involved peeling adhering specimens (50 mm × 25 mm × 2 mm) from the tissue surfaces and encapsulation/substrate materials of the devices (50 mm × 25 mm; various thicknesses for different materials). Films of PLA (thickness 50 μm) bonded to the specimens and the tissue samples minimized the contribution of elastic energy dissipation to the test results. The peeling rate was 60 mm min⁻¹. Twice the value of the plateau force divided by the width of the specimen yielded the adhesion energy. Peeling tests and the following tensile tests were performed using an MTS Sintech 20G and the data were collected using its recording software.

Mechanical properties. Tensile tests used unnotched and notched specimens (50 mm × 5 mm × 2 mm). Notched samples included a 25-mm-long crack from one edge to the middle, perpendicular to the stretching direction. The tensile rate was 15 mm min⁻¹. The slopes of stress-strain curves in the elastic zone of unnotched specimens defined the Young's moduli. The area under the stress-strain curves for unnotched specimens up to the strain at initial crack propagation defined the toughness⁴¹.

Rheology. The shear storage modulus served as a metric for characterizing the crosslinking density as a function of UV exposure time. Measurements used a modular compact rheometer (MCR302; Anton Parr) with a 25-mm-diameter cone plate (CP25) at an amplitude and angular frequency of 5% and 1 Hz, respectively. UV exposure began at 120 s and ended at 300 s. Data were collected using the RheoCompass software (Anton Paar).

Surface roughness. Analysis of surface roughness began with casting and curing a layer of BTIM on a sample of porcine skin without the use of primers. Carefully peeling the BTIM away from the porcine skin enabled measurements of the roughness of its interfacial surface. Scanning an area of 1.5 mm × 1.5 mm using a laser confocal microscope (LEXT OLS5000; Olympus) revealed the surface morphology and height distribution.

Transmittance. A UV/visible/near-infrared spectrophotometer (LAMBDA 1050; Perkin Elmer) defined the transmittance of specimens (25 mm × 25 mm × 2 mm) for wavelengths between 200 and 1,000 nm. Data were collected using UV WinLab software (LAMBDA 1050; Perkin Elmer).

Biodegradable behaviours. Evaluations involved gravimetric analysis, rheology and cryo-SEM (scanning electron microscope) imaging. Soaking BTIM specimens in PBS (pH 7.4, 37 °C) for a certain number of days, immersing these specimens in ultrapure water for 12 h to remove residual ions, and lyophilization (Labconco) enabled evaluation of the dried weights. The ratios of the dried weights to the original ones yielded the percentages of the remaining material, as a process of gravimetric analysis. Rheological measurements (MCR302; Anton Parr) from 0.1 to 100 Hz revealed changes of crosslinking density in specimens (diameter 25 mm; thickness 2 mm) at various times during degradation. Cryo-SEM imaging defined the corresponding changes in the microstructure. The process began with flash-freezing specimens using liquid ethane. A cryogenic transfer system (VCT100; Leica) shuttled the specimens in a vacuum coater (ACE600; Leica) to cool them to -120 °C. After freeze-etching for 5 min at -105 °C, depositing 7-nm-thick Pt on the surfaces of the specimens minimized charging for imaging in a cryo-SEM (S4800-II cold field-emission gun SEM; Hitachi) at -135 °C and a beam voltage of 5 kV.

Simulations. Commercial software (ABAQUS Analysis User's Manual 2010, V6.10) was used to study the stress distributions near the surfaces of biological tissues integrated with devices under typical loads, such as bending over and side-bending. The effects of the BTIM thickness (500 and 1,000 μm) and the device modulus (2 MPa and 2 GPa) were studied thoroughly. The coefficients of friction at the tissue-device interface and the tissue-BTIM interfaces were 0.15 and 0.05, respectively^{42,43}. The elastic modulus and Poisson's ratio were $E_{\text{tissue}} = 50$ kPa and $\nu_{\text{tissue}} = 0.5$ for tissue, $E_{\text{BTIM}} = 30$ kPa and $\nu_{\text{BTIM}} = 0.5$ for BTIM.

Commercial software (COMSOL 5.2a) in the electric current module (2D model; AD/DC Module User's Guide) was used to study the influence of BTIM conductivity on bioelectronic performance for electrical stimulation and

biopotential sensing. In both cases, the thickness, length and conductivity for biological tissues (myocardium) were 2 mm, 8 mm and 0.16 S m^{-1} , respectively. These parameters for BTIM were 0.5 mm, 8 mm and in the range between 0.001 and 100 S m^{-1} . For electrical stimulation, the parameters were chosen to be close to those in the applications of wireless pacemakers in a rat model. The pair of metal electrodes (material molybdenum; length 1 mm; thickness $50 \mu\text{m}$; spacing 3 mm) possessed a conductivity of $1.9 \times 10^7 \text{ S m}^{-1}$. A voltage of 3 V was applied to the electrodes for cardiac pacing. For biopotential sensing, the parameters were close to those in the applications of ultrathin MEA on the Langendorff-perfused rabbit heart. The eight electrodes of the MEA (material gold; length $500 \mu\text{m}$; thickness 300 nm ; spacing 1 mm) had a conductivity of $4.5 \times 10^7 \text{ S m}^{-1}$. A fixed potential (linear form; 1 V on the left endpoint and 0 on the right endpoint) was applied on the top surface of the myocardium layer. The internal resistance of the measurement set-up was considered to be $\sim 1\text{--}100 \text{ M}\Omega$. A convergence test of the mesh size ensured accuracy. The total number of elements in the models was approximately $\sim 700,000$.

Integration process for device arrays and 3D multilayer, electrode-embedded and electrode-exposed electronic systems. *Device arrays and multilayer structures.* Individually casting primers and precursor mixtures onto bare silicon chips coated with a layer of fluorescent acrylic paint and then placing them onto a sample of porcine skin, followed by UV exposure, yielded an array of 19 components in the shape of 'NU'. Repeating this process yielded a three-layer system.

3D electrode-embedded electronic systems. Fabrication began with spin-coating a layer of polyimide (PI, thickness $3 \mu\text{m}$) on a silicon wafer coated with a layer of polymethyl methacrylate. Depositing a bilayer of Cr/Au (thickness 10/100 nm) by electron beam evaporation, followed by photolithography (AZ5214; thickness $\sim 1.4 \mu\text{m}$) and wet etching, defined a pattern of electrodes. Eliminating the polymethyl methacrylate by immersion in acetone for 3 h allowed the transfer of the 2D structure from the silicon wafer to a water-soluble tape. Deposition of SiO_2 (thickness 100 nm) through a stencil mask (PI; thickness $\sim 10 \mu\text{m}$) by sputtering (AJA International) on the backside of the PI defined bonding sites. Exposing a prestretched silicone elastomer and the SiO_2 surface on the PI to UV ozone formed hydroxyl termination. Attaching the PI, as a 2D precursor, onto the stretched elastomer, followed by heating (60°C , 15 min) and releasing the prestrain, yielded the desired 3D configuration. Applying precursor mixtures to fully embed the 3D structure, followed by UV exposure and removal from the substrate, yielded a 3D free-standing electrode-embedded electronic system. Spreading primers and extra precursor mixtures on the surfaces of the device and the biological tissues enabled strong bonding. Impedance measurements over frequencies between 1 and 10^5 Hz utilized a commercial potentiometer (Autolab PGSTAT128N; Metrohm) with an Ag/AgCl reference. Data were collected using an Autolab NOVA v2.1.4 (Metrohm).

3D electrode-exposed electronic systems. Fabrication began with patterning a layer of PLA (thickness $\sim 50 \mu\text{m}$) by laser cutting (ProtoLaser R; LPKF Laser & Electronics). Depositing Cr/Au (thickness 5/50 nm) through a stencil mask (PI; thickness $\sim 10 \mu\text{m}$) by electron beam evaporation (AJA International) defined the pattern of electrodes. Deposition of SiO_2 (thickness 100 nm) through another stencil mask (PI; thickness $\sim 10 \mu\text{m}$) by sputtering (AJA International) on the backside of the PLA defined bonding sites. Exposing a prestretched silicone elastomer and the SiO_2 surface on the PLA to UV ozone formed hydroxyl termination. Attaching PLA, as a 2D precursor, onto the stretched elastomer, followed by heating (60°C , 15 min) and releasing the prestrain, yielded the desired 3D configuration with exposed electrodes on the surface. Injecting precursor mixtures inside the 3D structure, followed by UV exposure, created an electrode-exposed electronic system. The precursor mixtures filled the interior space due to capillary interaction. Removing this system from the silicone elastomer, coating it with primers and precursor mixtures and then exposing to UV allowed for integration with biological tissues.

In vitro cytocompatibility. A mouse cell line (ATCC CCL-1, L-929) was used for characterizing cell migration into the BTIM. A mixture of MEM (ATCC 30-2003), 10 vol.% fetal bovine serum (Thermo Fisher Scientific) and 1 vol.% penicillin-streptomycin (Thermo Fisher Scientific) served as the cell culture medium. The cells were maintained and cultured in a six-well cell culture insert (Thermo Fisher Scientific). Placing a matrix of the BTIM (diameter 2 cm; thickness $500 \mu\text{m}$) with platelet-derived growth factor (concentration 16 ng ml^{-1} ; Sigma-Aldrich) into the medium, which was replaced every 2 d, led to ingrowth. After 1 week, immersing the specimen in formaldehyde (4 vol.% in PBS: 0.1 M, pH 7.4; Sigma-Aldrich) at room temperature for 30 min fixed the adhesive matrix. Rinsing with PBS (0.1 M, pH 7.4) three times removed the formaldehyde. Incubating the adhesive matrix in Triton X-100 (0.1 vol.% in PBS: 0.1 M, pH 7.4; Sigma-Aldrich) at room temperature for 5 min permeabilized the cell membrane. The adhesive matrix was then blocked with BSA (1 vol.% in PBS: 0.1 M, pH 7.4) at room temperature for 1 h. After removing the BSA by rinsing with PBS (0.1 M, pH 7.4) three times, staining the adhesive matrix with F-actin marker rhodamine-phalloidin (Thermo Fisher Scientific) at room temperature for 40 min, followed by counterstaining with 4',6-diamidino-2-phenylindole (DAPI; Thermo Fisher Scientific) for 10 min, enabled imaging through a Leica SP8 confocal microscope and Hitachi SU8030 scanning electron microscope to observe the cell morphology in the

adhesive matrix. Before SEM imaging, the cells in the matrix were fixed using glutaraldehyde (2.5 vol.% in PBS: 0.1 M, pH 7.4) at 4°C for 2 h. The matrix was dehydrated in graded alcohol of 30%, 50%, 60%, 70%, 80%, 90%, 95% and 100%, and finally was dried with CO_2 in a critical point dryer. The specimen was sputter-coated with Os (thickness $\sim 10 \text{ nm}$) before observation. Images were captured and data were analysed using Gen5 software (BioTek Instruments).

Sterile processes for animal studies. Microfiltered and lyophilized SA and high-purity chitosan were dissolved in ultrapure water (0.5 wt%), sterile filtered (220-nm-diameter membrane pores), frozen at -20°C for 3 h and then lyophilized (Labconco) for 6 h. After lyophilization, the sterile alginate and chitosan were stored at -20°C before usage. The other chemicals, including PEG- α LA-DA, CaCl_2 , Irgacure D-2959, EDC and Sulfo-NHS were sterilized by filtering immediately before use. The synthesis process was performed in a tissue culture hood, and the precursor solutions were stored in 3-ml-volume syringes. External equipment, involving surgical tools, adaptors and UV lamps, were wiped with cloths soaked in 75% ethanol. All components and devices were sterilized using the ethylene oxide gas method.

Animals for in vivo characterizations. Animal procedures were performed according to protocols approved by the institutional animal care and use committees at Northwestern University and The George Washington University, and conformed to the Guide for the Care and Use of Laboratory Animals. For the studies on dorsal subcutaneous tissues and brains, young adult male and female C57BL/6 mice (postnatal days 60–80; weight $\sim 20 \text{ g}$) were used. Mice were maintained at $\sim 25^\circ\text{C}$ and humidity ranging from 30% to 70%, on a standard 12 h light–12 h dark cycle (lights on at 6:00 or 7:00) and fed ad libitum. Mice were group-housed (two to four per cage) before surgery, after which mice were individually housed in a climate-controlled vivarium. Approximately equal numbers of males and females were used. For cardiac studies, Sprague Dawley or Long Evans adult rats of both sexes (weight 300–600 g) were used. Rats are housed at 72°F and a humidity between 30% and 70% on a standard 12 h light–12 h dark cycle. For ECG mapping, female New Zealand white rabbits (3–6 months old) were used for the study. Rabbits are housed at 72°F and a humidity between 30% and 70% on a standard 12 h light–12 h dark cycle.

Surgical procedures for wireless devices for dorsal subcutaneous implantation. The devices consisted of wireless, battery-free miniaturized optoelectronic systems based on NFC technology ($\sim 10 \text{ mm} \times 6 \text{ mm} \times 300 \mu\text{m}$; 1 mm at the thickest regions). Mice were anaesthetized with isoflurane (induction value 3%; maintenance value 1.5–2%), received ketoprofen (5 mg kg^{-1} , intraperitoneal) for analgesia and were placed on a small-animal stereotaxic frame (David Kopf Instruments) for the surgery. Puralube veterinary ointment (Dechra Veterinary Products) was applied to cover the eyes during this procedure. A 1-cm-long incision was made over the shaved back to expose the subcutaneous tissues. The device was then placed on the subcutaneous tissue, followed by a PDMS mould to control the spread of the liquid precursor mixture. UV exposure followed the application of primers and precursors into this mould, and directly onto the device and adjacent regions of the tissue. After implantation, nylon 6-0 monofilament (Ethicon) sutures were applied to close the wounds, with standard post-surgical recovery procedures.

Evaluation of adhesive bonds for dorsal subcutaneous devices. *Positional stability by MicroCT analysis.* MicroCT imaging performed on different post-surgical days determined the positional stability of these devices. Mice were anaesthetized in an induction chamber with 3% isoflurane in oxygen and transferred to a dedicated imaging bed with isoflurane delivered via a nosecone at 1–2%. The mouse was placed in the prone position in a dedicated chamber with the head immobilized using ear and tooth bars. Respiratory signals were tracked using a digital monitoring system (Mediso-USA). Images were acquired at $\times 2.17$ magnification, using a $33 \mu\text{m}$ focal spot, 1×1 binning, 720 projection views over a full circle, a 300 ms exposure time and 70 kV_p . The projection data were reconstructed with a voxel size of $68 \mu\text{m}$ using filtered (Butterworth filter) back-projection software from Mediso. The reconstructed data were visualized in Amira version 2020.3 (FEI). MicroCT images were manually registered, since artifacts caused by the device precluded automatic image registration.

Measurement of device translation. All analysis was performed using Amira version 2020.3. MicroCT scans, which were modified using a non-local means filter, segmented the device at each timepoint (days 2, 5 and 8 after surgery) with a combination of thresholding and manual segmentation. Cropping the skeleton of the mouse, segmented using a threshold of 700 Hounsfield units, resulted in a region of interest containing only L3, L4 and L5. The vertebral segments from the second and third timepoints were automatically registered to the vertebral segment from the first timepoint using normalized mutual information. Each vertebral transform was copied to its corresponding device so that all devices were registered to the vertebrae from the first timepoint. The device regions of interest were binarized using an automated adaptive thresholding tool, and the centroid of each device was noted.

Evaluation of functionality of dorsal subcutaneous devices. *Optical characterization.* A commercial radiofrequency system (NeuroLux) wirelessly

delivered power to activate the devices. Visual observation of light from the ILED enabled inspection for device functionality every 2 d. The mice with implants roamed freely within an enclosed cage encircled by a loop antenna connected to a laptop with a software control interface to a power distribution control box and an antenna tuner box (NeuroLux). The cage, equipped with a wireless system, allowed mice to move freely without tethers. A mobile phone with NFC capability placed close (<1 cm) to the dorsal subcutaneous tissues provided an alternative means to initiate the illumination. Evaluations were performed for 2 months or until the devices ceased to function.

Evaluation of biocompatibility for BTIM-encapsulated dorsal subcutaneous devices. *Locomotor characterization.* The tests involved studies of locomotor activity of mice with and without implanted devices (experimental and control groups, respectively). The trials began with placing mice one at a time in the centre of a plastic chamber (48 cm × 48 cm × 40 cm) in a dimly lit room. Animals explored the arena for 15 min, with video (30 frames per second) capture of their behaviour during the final 5 min using a Raspberry Pi camera v2 (Raspberry Pi Foundation). Comparison of the trajectories of locomotor behaviours and statistical evaluations of the distance travelled in each session relied on monitoring the body centre of the animal using ToxTrac v2.90⁴⁴.

Immunofluorescence staining. Animals implanted with the BTIM were killed at weeks 1, 3, 5 and 7 after surgery. 10- μ m-thick dorsal epidermal tissue sections were collected using a CMI1850UV Cryostat (Leica). Rinsing tissue sections with PBS (0.1 M) at room temperature for 30 min removed the optimum cutting temperature compound. Fixing with formaldehyde (4 vol.% in PBS: 0.1 M, pH 7.4; Sigma-Aldrich) at room temperature for 30 min, followed by rinsing with PBS (0.1 M, pH 7.4) three times, removed formaldehyde. Incubating with Triton X-100 (0.1 vol.% in PBS: 0.1 M, pH 7.4; Sigma-Aldrich) at room temperature for 10 min permeabilized the cell membrane. After three cycles of rinsing with PBS (0.1 M, pH 7.4), the tissue sections were blocked with BSA (1 vol.% in PBS: 0.1 M, pH 7.4) at room temperature for 1 h. Two kinds of primary antibody for macrophage (CD68+, 0.5%, and CD163+, 0.5%; Abcam) were utilized to incubate the tissue sections at 4 °C for 12 h. After three cycles of rinsing with PBS (0.01 M, pH 7.4), the tissue sections were further incubated with the secondary antibodies (goat anti-mouse 488 and goat anti-rabbit 568; Abcam). Applying DAPI (Thermo Fisher Scientific) as a fluorescent stain counterstained the cell nucleus. Micrographs were obtained with an SP8 confocal microscope (Leica).

Haematoxylin and eosin staining. Mice were deeply anaesthetized with isoflurane and transcardially perfused with 10% neutral buffered formalin. Back tissue was post-fixed for 7 d before processing and sectioning. Standard protocols for haematoxylin and eosin staining were followed. Four-micrometre-thick tissue sections adhered to slides were dewaxed and cleared with xylene, hydrated through incubation in a series of decreasing concentrations of alcohols (100–70%), stained with filtered haematoxylin, treated with an alkaline solution and counterstained with eosin. Subsequently, sections were dehydrated in several changes of alcohol, cleared and coverslipped. Sections were imaged using an Olympus VS120 microscope in bright-field mode. Coloured bright-field images of back tissue sections were automatically acquired and stitched using an automated slide scanner and a ×20 objective. Analysis was carried out in Fiji^{45,46} using line and area measurement. The same analysis parameters were applied across all regions of interest.

Surgical procedures for wireless devices for deep-brain optogenetics. The devices consisted of wireless optogenetic platforms based on NFC technology for untethered neuronal control and discrete spatiotemporal targeting of neural circuits. The constituent components included a penetrating probe with a μ -ILED at its tip end for insertion into the deep brain and a receiver coil for wireless power harvesting above the skull in the subcutaneous tissues. The fabrication process followed procedures described previously²¹. Standard anaesthesia and eye protection of mice proceeded as described above. A 5-mm-long incision made on the scalp exposed the skull and allowed for drilling a hole to insert the probe into the targeted brain regions. Coordinates for medial prefrontal cortex probe placement were +2.0 mm (anterior–posterior), +0.4 mm (medial–lateral) and +1.5 mm (dorsal–ventral). The BTIM encapsulated the receiver coil and anchored the platform onto the skull. A 6-0 nylon monofilament (Ethicon) suture closed the wound after implantation.

Evaluation of adhesive bonds and device functionality of deep-brain optoelectronics. *Optical stimulation.* Every 2 d, the implanted devices were wirelessly powered by a commercial radiofrequency system (NeuroLux) to activate the optical stimulation as an assessment of device functionality. The devices remained functional throughout the 2 week period before killing the animals. The optoelectronic systems remained firmly adhered to the skull throughout this time.

MicroCT and MRI. Evaluations of device position 2 weeks after surgery were performed using MicroCT and MRI analysis. For MicroCT, see the procedures described previously. MRI was performed on a 9.4 T Bruker BioSpec MRI system

with a 30 cm bore, a 12 cm gradient insert and an AutoPac automated sample positioning system (Bruker BioSpin). Respiratory signals were recorded using an MR-compatible physiologic monitoring system (SA Instruments). A warm-water circulating system maintained body temperature. An actively decoupled, four-channel phased array, receive-only radiofrequency coil designed specifically for the mouse brain (Bruker BioSpin) was mounted on the bed. This assembly was centred inside a 72 mm quadrature volume coil in transmit-only mode (Bruker BioSpin). Mice were imaged using an accelerated spin-echo sequence (turbo rapid acquisition with relaxation enhancement, TurboRARE) oriented in axial, sagittal and coronal directions. The following parameters were used: repetition time/echo time 1,250 ms/21.3 ms, RARE factor 8, matrix 256 × 256, field of view 3 cm × 3 cm, 7–13 slices 0.75–1 mm thick (as needed for full brain coverage), flip back enabled and three signal averages. The acquisition time was approximately 2 min per scan.

Evaluation of biocompatibility of BTIM-encapsulated deep-brain optoelectronics. *Tissue processing and immunohistochemistry.* Mice with BTIM implantation were deeply anaesthetized with isoflurane and transcardially perfused with 4% paraformaldehyde. The brain was extracted and post-fixed for 1–5 d before sectioning. 60- μ m-thick sections were collected and incubated with rabbit anti-GFAP (1:1,000; Abcam) and rabbit anti-IBA1 (1:1,000; Abcam), as described in previous studies^{47,48}. On the following day, tissues were rinsed three times with PBS, reacted with anti-rabbit Alexa Fluor 647 secondary antibody (1:500; Thermo Fisher Scientific) for 2 h at room temperature and rinsed again three times in PBS. Sections were mounted on SuperFrost Plus slides (Thermo Fisher Scientific), air dried and coverslipped under glycerol:Tris-buffered saline (9:1) with Hoechst 33342 (2.5 μ g ml⁻¹; Thermo Fisher Scientific). Whole sections were imaged with an Olympus VS120 slide-scanning microscope. Analysis was carried out in Fiji^{45,46} using autothresholding and area measurement. The same analysis parameters were applied across all regions of interest.

Surgical procedures for bioresorbable optical filters for the brain. The optical filters consisted of bioresorbable multilayers of silicon dioxide (SiO₂; thickness of each layer 54 nm) and silicon nitride (SiN_x; thickness of each layer 85 nm) on a layer of PLGA (thickness ~10 μ m). The fabrication process followed those of a previous study³². Standard anaesthesia and surgical procedures were similar to those described above. A 5-mm-long incision made on the scalp exposed the skull, to allow removal of a section (3 mm × 3 mm) for alignment and insertion of the filter onto targeted regions of the brain. The filter encapsulated with the BTIM touched the exposed cerebral area to modulate the transmission (wavelength 520–900 nm) and reflection (wavelength 450–520 nm) spectra for characterization of neural calcium transients based on GCaMP. A commercial fibre-optic spectrometer (Ocean Insight) measured the reflection spectrum of the optical filter.

Evaluation of adhesive conduits for interconnects/cables. These studies focused on interconnects/cables as electrical interfaces between devices for sensing/stimulating in deep tissues and receivers and other hardware for power supply, wireless communications and other functions in subcutaneous tissues. The fabrication process began with photolithographic patterning of multilayer serpentine structures, consisting of parylene/Ti/Cu/Ti/Au/parylene (thicknesses 5 μ m/20 nm/300 nm/20 nm/50 nm/5 μ m), followed by transfer onto a silicone elastomer (Ecoflex 00-30) using a water-soluble tape (AquaSol Corporation). The surgical procedures are the same as those for dorsal subcutaneous devices. After anchoring the interconnect with an adhesive conduit, stretching tests were performed with a pair of forceps to grasp the uncovered end. The mice were posed gently to bend the interconnect as a test of bending stability.

Ex vivo characterization of devices designed to interface with moving tissue surfaces. Evaluations of adhesion to wet, dynamic tissues used bioresorbable, wireless, battery-free, miniature pacemakers. The fabrication process followed steps described previously²². Ex vivo characterization involved an isolated chicken heart fixed on a modified vibration stage moving at 20 Hz with an amplitude to mimic the cyclic movement of a beating heart. Anchoring the pacing electrodes onto the surface of the heart with the BTIM during these motions demonstrated the ability to bond to a wet and dynamic curvilinear tissue surface. Soaking the entire system in PBS (pH 7.4) at 25 °C for 2 weeks validated the stability of this bond.

Surgical procedures for wireless systems designed for cardiac pacing. Fully implantable, bioresorbable, wireless, battery-free pacemakers were implanted into male and female adult rats (Sprague Dawley and Long Evans). All surgeries were performed under general anaesthesia with isoflurane. Each rat's ECG was recorded using a PowerLab acquisition system and LabChart software (ADInstruments) in the standard lead I configuration (left arm as the negative electrode, right arm as positive and right leg as ground) to monitor the heart rate throughout the procedure. Animals were intubated with a 16-gauge blunt-tip catheter and ventilated using a VentElite small-animal ventilator (Harvard Apparatus). The heart was exposed via the left thoracotomy. For animals in which the BTIM was used, the electrodes of the pacemaker were specially outfitted with a rectangular PLGA frame to allow for full contact between the electrodes and the tissue when placed onto the anterior epicardial surface. The primers and precursors

were spread into the PLGA frame and polymerized by UV exposure for 3 min. For control animals that had the devices implanted using sutures, the electrode pad of the pacemaker was sutured onto the anterior epicardium using two interrupted monofilament sutures (Ethicon). The receiver of the pacemaker was placed into a subcutaneous pocket on the ventral aspect of the animal. The thoracic cavity, muscle and skin were then closed in the ensuing layers using 6-0 nylon monofilament sutures (Ethicon). Pacing and capture of the heart to verify pacemaker functionality were confirmed by ECG signals immediately after device attachment and following closure. Animals were allowed to recover until recumbency was regained. Analgesic was provided every 12 h in the 48 h following surgery, along with appropriate postoperative care.

Evaluation of adhesive bonds and device functionality for cardiac pacing devices. Power was delivered to the pacemaker via wireless inductive power transfer. During each pacing session, a three-lead ECG in the lead I configuration was recorded using LabChart software (ADInstruments). Heart rate was calculated from cyclic measurements of the R wave from the ECG. The resting heart rate in these cohorts was approximately 350 b.p.m. During implantation, animals were paced immediately following the deployment of the BTIM onto the heart and after the closure of muscle and skin. Post-operatively, animals were subjected to ventricular pacing at 400 b.p.m. or higher, and an ECG was recorded to assess the device functionality. The pacing was performed until the pacemaker failed to drive the heart rhythm. Explanting the hearts that had pacemakers implanted with the BTIM 10 d after surgery enabled observations and assessments of the level of adhesion. Stable and firm adhesion 10 d after surgery was verified by device explantation. A qualitative test of suspending and mechanically agitating the heart was employed to affirm the level of delamination between electrodes and the heart.

Evaluations of biocompatibility for BTIM-encapsulated cardiac pacing devices.
Histological analysis. Growth of fibrotic tissue was evaluated for rats without implanted devices, with pacemakers implanted using sutures and with pacemakers implanted using the BTIM. Four weeks after implantation, hearts were excised and perfusion-fixed with 10% neutral buffered formalin. Tissue samples were then paraffin-embedded, sectioned and stained with Masson's trichrome. Images were collected at $\times 4$ magnification using an EVOS XL light microscope (Thermo Fisher Scientific). The volume fractions of myocytes, collagen and interstitial space were assessed for the transmural volume near the site of device attachment through MATLAB (MathWorks). Personnel performing analysis were blinded to group allocations. The amount of disorganized connective tissue on top of the myocardium, as observed during explantation, was evaluated by a double-blinded clinical-scoring system on a scale of 0 to 5. The scoring system was scaled as follows: no signs of scarring (0), minimal amount of transparent scarring that is easily disrupted (1), small amount of scar tissue that requires blunt instruments to disrupt (2), moderate amount of opaque scarring that requires blunt instruments to disrupt (3), dense scar tissue that requires sharp instrumentation to disrupt (4) and very dense scar tissue that grossly distorts heart anatomy (5). A Kruskal–Wallis statistical test was used to compare volume fractions and clinical score outcomes between the control, suture and BTIM groups, where $*P \leq 0.05$ was considered statistically significant.

MicroCT and MRI analysis. All procedures, including data visualization and image registration, were similar to those previously described for deep-brain optogenetics.

Fabrication process for systems designed for cardiac electrophysiology mapping. A thin, flexible electrode array with 64 channels served as the platform for cardiac electrophysiology mapping. The fabrication process began with coating a layer of parylene (thickness 4 μm) on a glass slide. A lift-off process defined patterns for the electrodes and interconnects in Cr/Au (thicknesses 10/100 nm). Deposition of another layer of parylene (thickness 4 μm) covered the metal pattern. Photolithography (AZ4620; thickness $\sim 10 \mu\text{m}$) and oxygen plasma etching (MARCH RIE) removed regions of the parylene to expose the metal electrodes. Carefully peeling the electrode array from the glass substrate after thermally anchoring a 15-cm-long anisotropic conductive film on the connection pads completed the process.

Surgical procedures for systems designed for cardiac electrophysiology mapping. All animal procedures were performed according to protocols approved by the George Washington University Institutional Animal Care and Use Committee. Rabbits were first anaesthetized with a mixture of ketamine and xylazine, and isoflurane vapours were administered to deepen the anaesthesia further. A dose of heparin was administered intravenously by ear vein injection. Cessation of pain was confirmed via toe pinch, and then the heart was excised via sternal thoracotomy. The heart was immediately cannulated in University of Wisconsin cardioplegia solution via the aorta and placed into a constant-pressure Langendorff system perfused with a modified Tyrode solution (mM: 128.2 NaCl, 4.7 KCl, 1.05 MgCl_2 , 1.3 CaCl_2 , 1.19 NaH_2PO_4 , 20 NaHCO_3 and 11.1 glucose) at 37 °C that was bubbled with 95% O_2 –5% CO_2 . The heart was allowed to

recover for 5–10 min. Following the recovery period, the excitation–contraction uncoupler blebbistatin (Cayman Chemical) was administered so that the working concentration in the system was at 10 μM . A voltage-sensitive dye (125 nM), di-4-ANEPPS (excitation/emission wavelengths 520/650 nm), was added at an upstream bubble trap to stain the tissue. As a control, the ultrathin, flexible 64-electrode array was applied with no adhesive encapsulation or adhesive interface to the heart.

For the encapsulation method, the electrode array was first placed on the epicardium, and then the primer and precursor mixtures were applied to coat the device to the adjacent tissue. Exposure to UV light cured the BTIM. For the interface method, forming amine functional groups on the parylene surfaces of the device followed the procedures mentioned above. Applying primer and precursor mixture onto the epicardium, placing the array on top and then exposing to UV completed the process.

Evaluation of functionality of devices for cardiac electrophysiology mapping. After applying the BTIM by the encapsulation or interface methods, connections between the array and an Intan 1,024-channel recording controller were made through two 36-pin wire adaptors, a 64-channel amplifier board (RHD2164) and a serial peripheral interface cable via a 15-cm-long anisotropic conductive film, a laser-defined printed circuit board, a zero-insertion-force interconnector and another customized printed circuit board. A commercial software interface simultaneously recorded electrograms across all 64 channels at a sampling rate of 20 kS s^{-1} , across a frequency range of 0.1–200 Hz with a notch filter at 60 Hz. A high-speed CMOS (complementary metal–oxide–semiconductor) camera with the MiCAM05 system (SciMedia) optically mapped the cardiac tissue membrane potential (sampling frequency 1 kHz) by exciting the voltage-sensitive dye-stained tissue using a 520 nm green light (Prizmatix). Passing a digital pulse from the MiCAM05 to the Intan system triggered synchronized recording of the electrical signals and optical signals with the respective systems.

Statistical analysis. Statistical significance and P values of Fig. 3k, Extended Data Fig. 6b,c and Supplementary Figs. 17 and 18 were determined with two-sided Student's t -tests using Microsoft Excel. Statistical significance and P values of Fig. 5f,g were determined with a Kruskal–Wallis test and post hoc Dunn multiple-comparison test using Statsoft. Statistical significance and P values of Fig. 6f,g were determined with a Wilcoxon matched pairs signed-rank test using Statsoft. Statistical significance and P values of Extended Data Fig. 2f are determined with one-way analysis of variance using GraphPad Prism. The significance thresholds were $*P \leq 0.05$. NS indicates no statistically significant differences.

Reporting Summary. Further information on research design is available in the Nature Research Reporting Summary linked to this article.

Data availability

Source data are provided with this paper. All other data that support the results in this study are available from the corresponding author upon reasonable request.

Code availability

Software for the analysis of optical mapping data, RHYTHM, is openly available for free download at <https://github.com/optocardiography>. Other custom codes used in this study are available from the corresponding author upon reasonable request.

References

- Sawhney, A. S., Pathak, C. P. & Hubbell, J. A. Bioerodible hydrogels based on photopolymerized poly(ethylene glycol)-co-poly(α -hydroxy acid) diacrylate macromers. *Macromolecules* **26**, 581–587 (1993).
- Park, y. et al. Three-dimensional, multifunctional neural interfaces for cortical spheroids and engineered assembloids. *Sci. Adv.* **7**, eabf9153 (2021).
- Sun, J.-Y. et al. Highly stretchable and tough hydrogels. *Nature* **489**, 133–136 (2012).
- Gong, J. P. et al. Synthesis of hydrogels with extremely low surface friction. *J. Am. Chem. Soc.* **123**, 5582–5583 (2001).
- Rudy, A. et al. Lubricous hydrogel surface coatings on polydimethylsiloxane (PDMS). *Tribol. Lett.* **65**, 3 (2017).
- Rodríguez, A. et al. ToxTrac: a fast and robust software for tracking organisms. *Methods Ecol. Evol.* **9**, 460–464 (2018).
- Schneider, C. A., Rasband, W. S. & Eliceiri, K. W. NIH Image to ImageJ: 25 years of image analysis. *Nat. Methods* **9**, 671–675 (2012).
- Schindelin, J. et al. Fiji: an open-source platform for biological-image analysis. *Nat. Methods* **9**, 676–682 (2012).
- Wu, M. et al. Attenuated dopamine signaling after aversive learning is restored by ketamine to rescue escape actions. *eLife* **10**, e64041 (2021).
- Wu, M., Minkowicz, S., Dumrongprechachan, V., Hamilton, P. & Kozorovitskiy, Y. Ketamine rapidly enhances glutamate-evoked dendritic spinogenesis in medial prefrontal cortex through dopaminergic mechanisms. *Biol. Psychiat.* **89**, 1096–1105 (2021).

Acknowledgements

This work was generously funded by the Leducq Foundation project RHYTHM and the National Institutes of Health (R01-HL141470 to I.R.E. and J.A.R.). This work made use of the NUFAB facility of Northwestern University's NUANCE Center, which received support from the Soft and Hybrid Nanotechnology Experimental (SHyNE) Resource (NSF ECCS-2025633); the MRSEC programme (NSF DMR-1720139) at the Materials Research Center; the International Institute for Nanotechnology (IIN); the Keck Foundation; the Querrey Simpson Institute for Bioelectronics; the Keck Biophysics Facility, a shared resource of the Robert H. Lurie Comprehensive Cancer Center of Northwestern University, which received support in part by the NCI Cancer Center Support (P30 CA060553); the Center for Advanced Molecular Imaging (RRID:SCR_021192); Northwestern University; and the State of Illinois, through the IIN. R.T.Y. acknowledges support from the American Heart Association (19PRE34380781). M.W. acknowledges support from the National Institutes of Health (T32 AG20506). Z.X. acknowledges support from the National Natural Science Foundation of China (12072057), LiaoNing Revitalization Talents Program (XLYC2007196) and Fundamental Research Funds for the Central Universities (DUT20RC(3)032). K.A. acknowledges support from the National Institutes of Health (5K99-HL148523-02). Y.H. acknowledges support from the National Foundation of Science (CMMI1635443). Y.K. acknowledges support from the National Institutes of Health (R01NS107539 and R01MH117111), Beckman Young Investigator Award, Rita Allen Foundation Scholar Award and Searle Scholar Award. The diagrams of the mouse body with organs in Fig. 1f were created with [BioRender.com](https://www.biorender.com).

Author contributions

Q.Y., T. Wei, Y.K., I.R.E. and J.A.R. conceived the ideas and designed the research. Q.Y., T. Wei, Y.X. and T.-L.L. synthesized and characterized the materials. Q.Y., Y.X., J.K., Y.S.C., W.B., Y.Y., M.H., Q.Z., T. Wang, M.-H.S., H.L., S.M.L. and A. Banks designed and fabricated the devices. R.T.Y., M.W., S.W.C., I.K., S.Y., C.R.H., K.B.L., K.A., A. Brikha, I.S., F.A., E.A.W. and G.D.T. performed the in vitro, ex vivo and in vivo studies. Q.Y., R.T.Y., Y.X., M.W., C.R.H., A. Banks and E.A.W. performed the data analysis. Z.X., R.A. and Y.D. performed the mechanical and electrical modelling. Q.Y., Y.X., R.T.Y., T.W., M.W., J.M.T., Y.H., Y.K., I.R.E. and J.A.R. wrote the manuscript with input from all authors.

Competing interests

The authors declare no competing interests.

Additional information

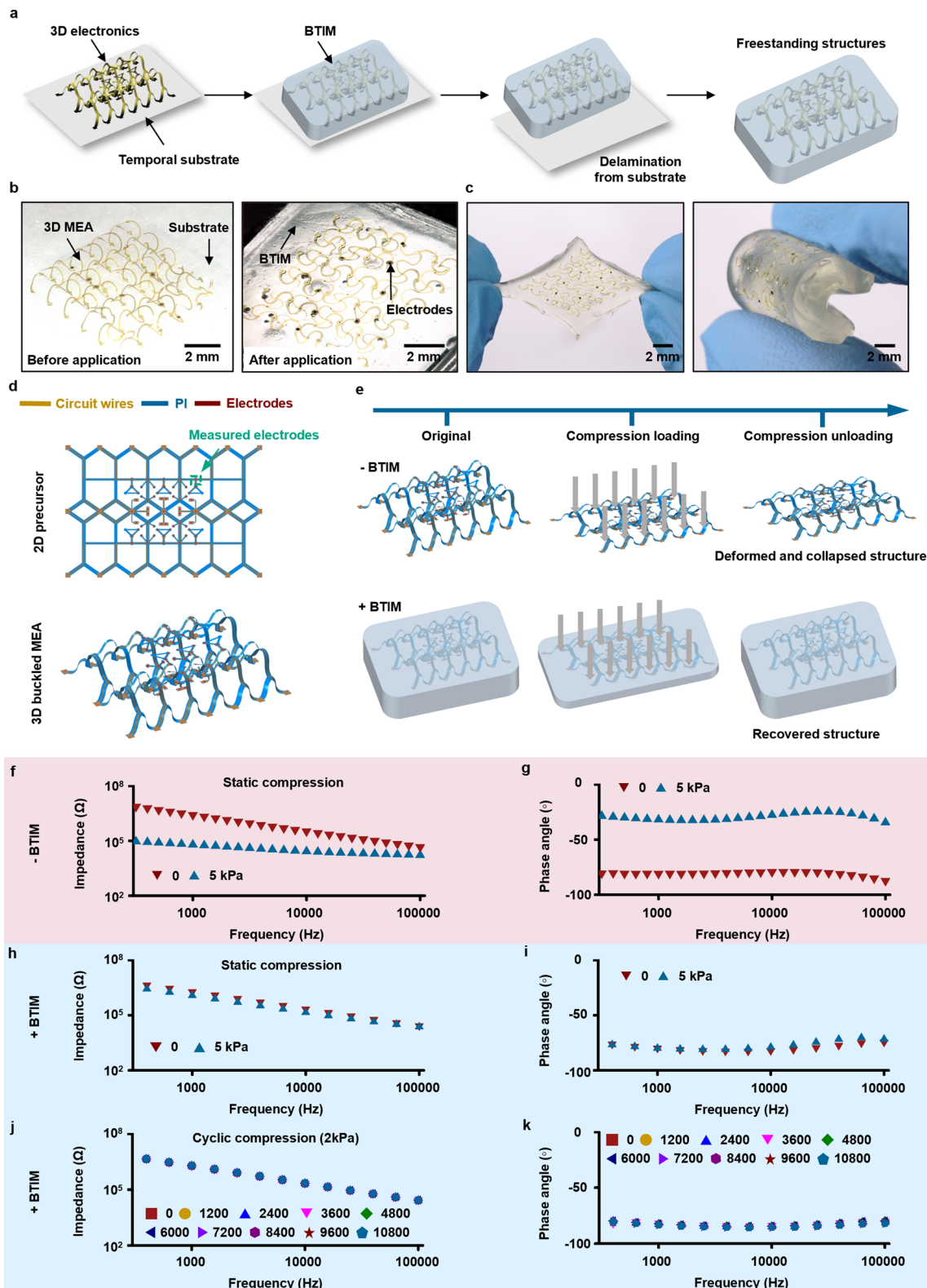
Extended data is available for this paper at <https://doi.org/10.1038/s41563-021-01051-x>.

Supplementary information The online version contains supplementary material available at <https://doi.org/10.1038/s41563-021-01051-x>.

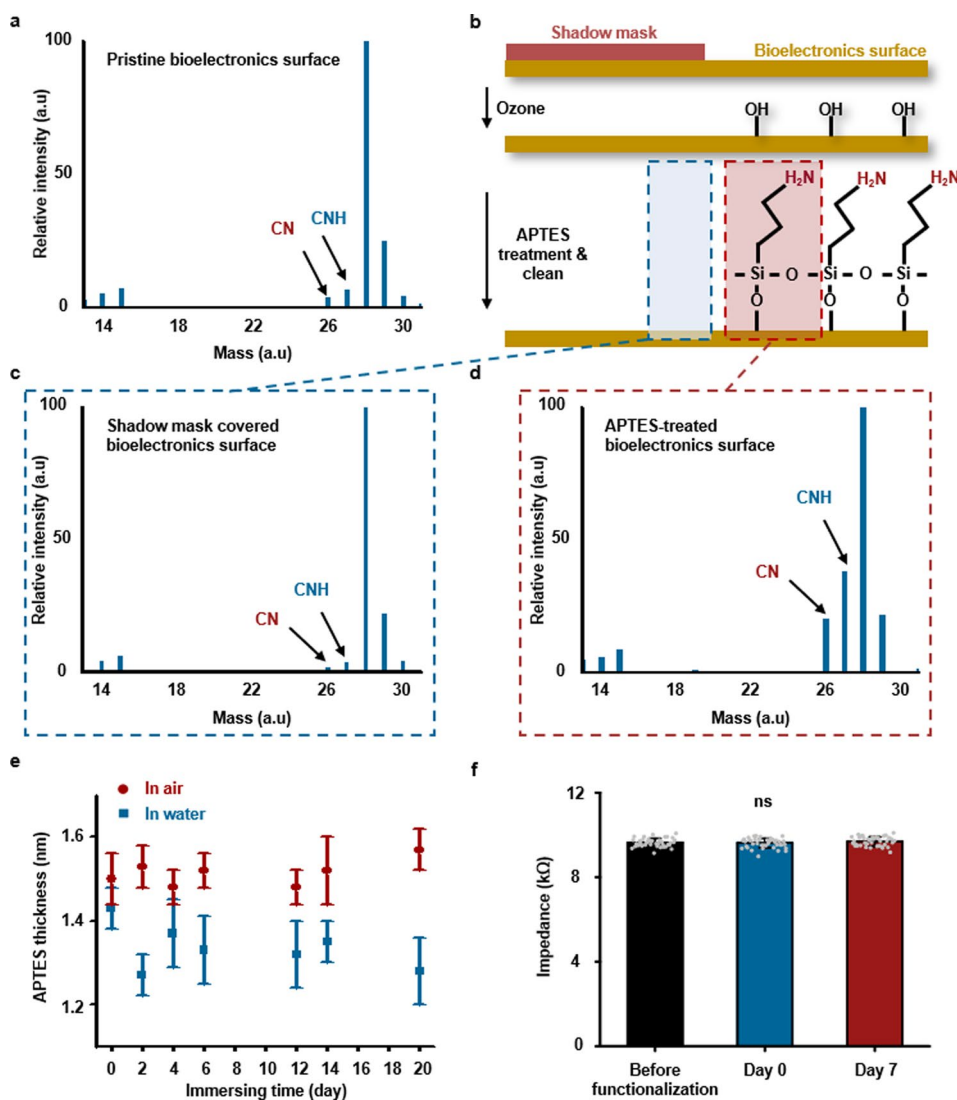
Correspondence and requests for materials should be addressed to Y.K., I.R.E. or J.A.R.

Peer review information *Nature Materials* thanks John Ho, Yuhan Lee, Tsuyoshi Sekitani and the other, anonymous, reviewer(s) for their contribution to the peer review of this work.

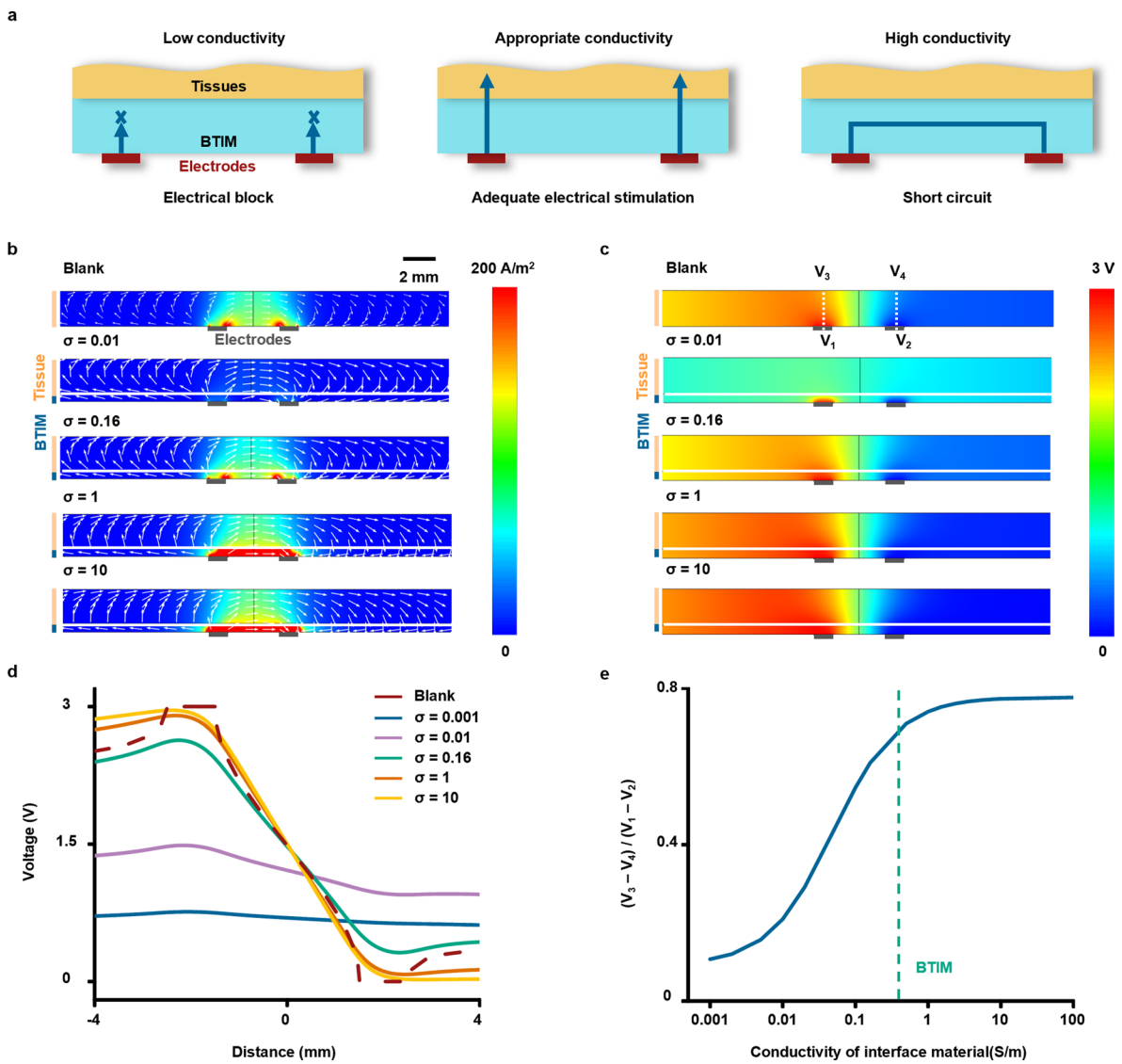
Reprints and permissions information is available at www.nature.com/reprints.



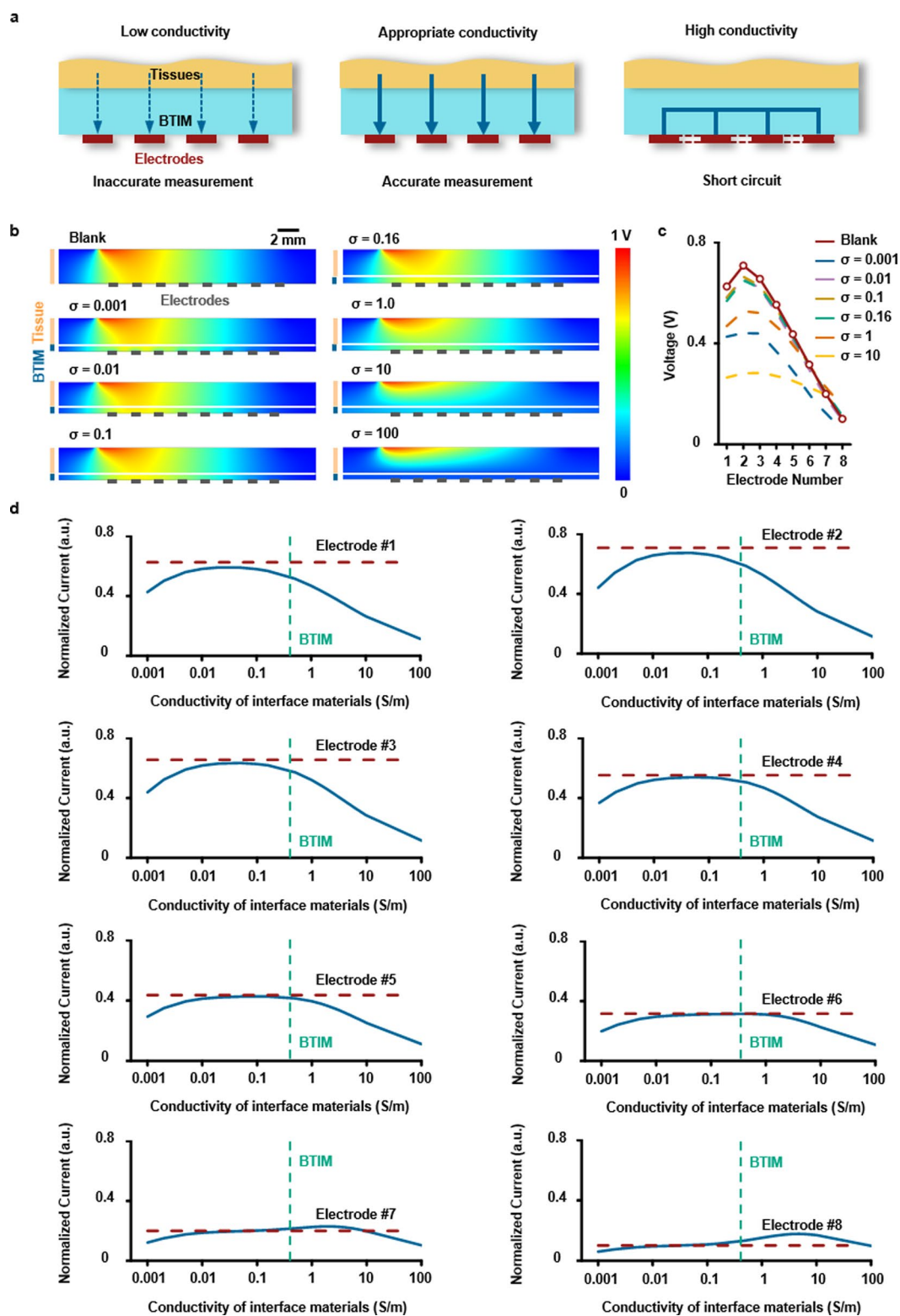
Extended Data Fig. 1 | Supporting matrices for electrode-embedded 3D electronic systems. **a**, Schematic illustration of procedures to integrate 3D electronics into a matrix of the BTIM. The matrix allows manual manipulation without damaging fragile features, with the ability to bond to dynamic, curved tissue surfaces. **b**, Image of a 3D device formed by compressive buckling on an elastomer substrate. **c**, Micrograph of a 3D device in a BTIM supporting matrix. **d**, Schematic illustrations of the 2D precursor before compressive buckling (first panel) and the 3D structure after compressive buckling (second panel), with the measuring electrode in the central area. **e**, Schematic illustration of the original and deformed status of the non-encapsulated (first row) and the BTIM-encapsulated (second row) 3D devices under compressive pressure. **f**, **g**, Curves for impedance and phase angle over the frequency sweep without the BTIM before and after compressive pressure. **h**, **i**, Impedance and phase angle over the frequency sweep with the BTIM under static compression fatigue tests. **j**, **k**, Impedance and phase angle over the frequency sweep with the BTIM under dynamic compression fatigue tests (pressure: 2 kPa; cycle number: 10^4).



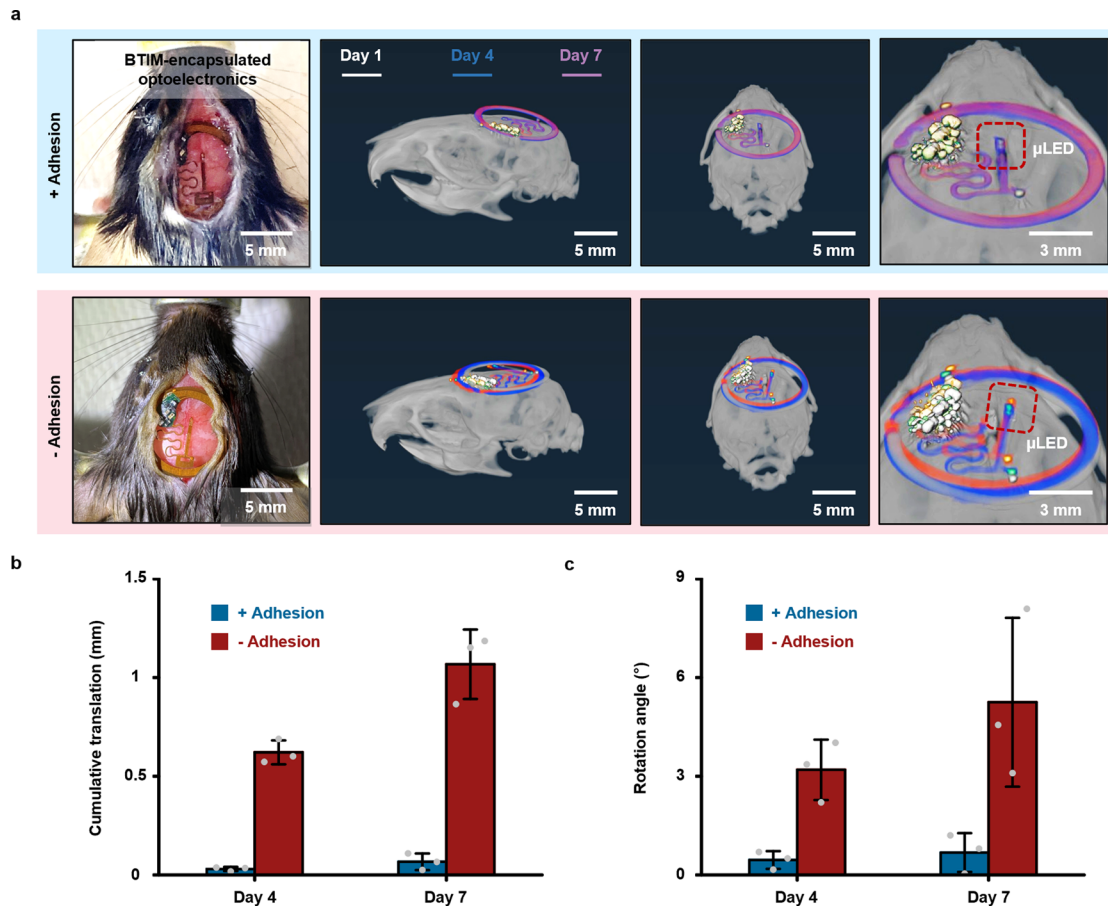
Extended Data Fig. 2 | Influence of APTES-functionalization on bioelectronics surfaces. **a**, ToF-SIMS analysis of a representative pristine bioelectronic surface (PLA). **b**, Steps for selective functionalization of this surface through a patterned polyimide adhesive-coated shadow mask. **c**, ToF-SIMS analysis on the shadowed area of the surface shows results that are similar to those from the pristine surface. **d**, ToF-SIMS analysis of the exposed area of the bioelectronic surface. To normalize the intensity, the intensity I_{28} , where the mass is 28, was set as 100 and calculate the relative intensity of each case. **e**, Thickness of an APTES layer formed on a silicon wafer exposed in air and submerged in water as a function of time after formation. Spectroscopic ellipsometry was used for these measurements. **f**, Impedance of MEA electrodes at 1 kHz in 0.1 M PBS at room temperature before APTES functionalization and immediately and 7 days after APTES functionalization ($F(2,123) = 0.0201$, $P = 0.9801$). $n = 6$ independent samples in **e** and $n = 40$ independent electrodes from 10 independent devices and 3 independent batches in **f**. Values in **e** and **f** represent the mean \pm s.d. Statistical significance and P values are determined by one-way ANOVA at a significance level of 0.05. ns indicates no statistically significant differences.



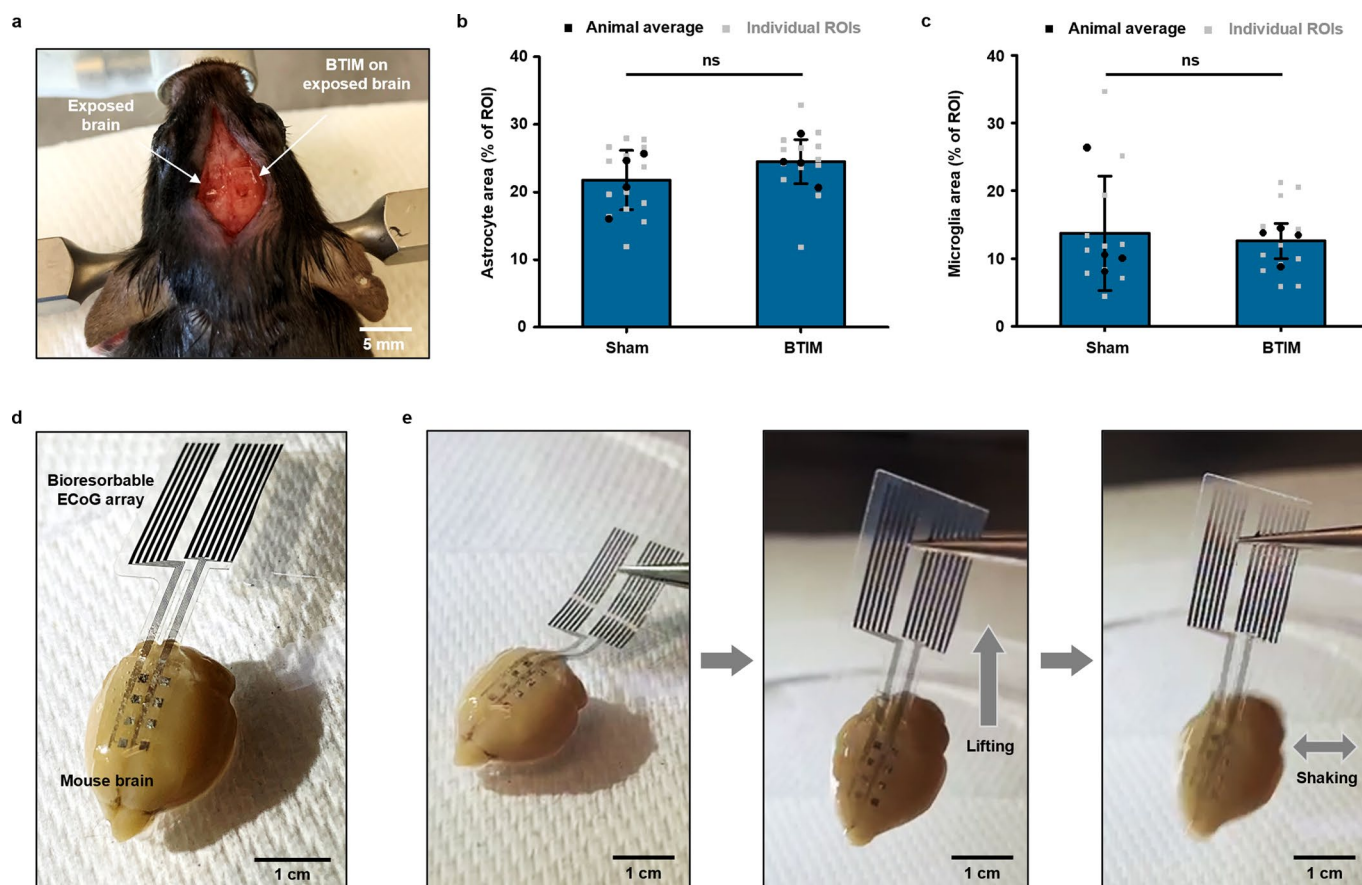
Extended Data Fig. 3 | Analysis of the electrical distributions associated with electrical stimulation. a, Influence of the conductivity of the interface material on electrical stimulation. **b**, Current density distributions in the myocardium layer and the interface material with different conductivities. **c**, Potential distribution in the myocardium layer and the interface material with different conductivities. **d**, Corresponding potential distributions on the top of the myocardium layer as a function of the interface material conductivity. **e**, Ratio of the potential difference on the tissues ($V_3 - V_4$) to the corresponding potential difference on the electrodes ($V_1 - V_2$, 3 V) as a function of the interface material conductivity.



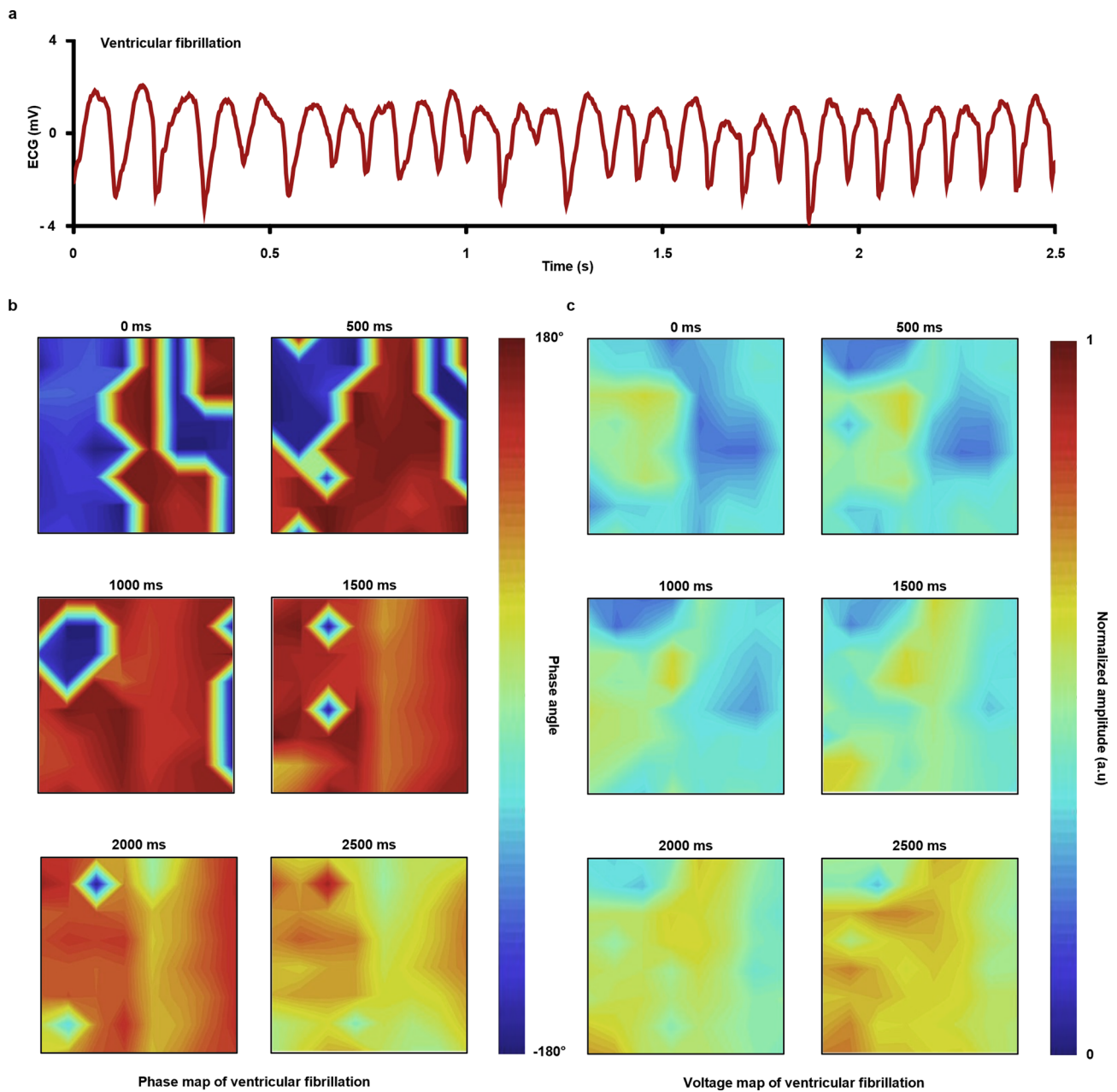
Extended Data Fig. 4 | Analysis of the electrical distributions associated with biopotential mapping. **a**, Influence of the conductivity of the BTIM on biopotential mapping. **b**, Biopotential distribution in the myocardium layer and the interface material layer with various conductivities. **c**, Calculated potential at all of the electrodes for different conductivities. **d**, Calculated potential on all the electrodes in the presence of the interface material layer with various conductivities (blue solid line) and in the absence of the interface material layer (red dash line).



Extended Data Fig. 5 | Mechanical stability of BTIM-encapsulated wireless optoelectronics. **a**, Original device position determined by photographs, and positions of BTIM-encapsulated devices (first row) and non-adhesive (second row) devices on day 1 (white), 4 (blue), and 7 (purple) post-surgery determined by MicroCT. **b**, **c**, Statistical analyses of the net translations (**b**) and rotations (**c**) of the μ -LED in the BTIM-encapsulated (blue) and non-adhesive devices (red) on day 4 and 7 compared with those on day 1 post-surgery. $n=3$ biologically independent animals. Values in **b-c** represent the mean \pm s.d.



Extended Data Fig. 6 | Applying BTIM on brain-integrated bioelectronics/optoelectronics. **a**, Image of the brain areas exposed to the BTIM. **b, c**, Astrocyte area percentages and microglia area percentages for the sham group and the BTIM group. Black dots: animal average, 4 animals in total. Grey dots: individual ROIs. 10–12 ROIs from 4 animals in total, 2–3 ROIs from each animal. $P=0.3546$ in **b** and $P=0.8049$ in **c**. **d**, The image of the BTIM-encapsulated b-MEA on a mouse brain ex vivo. **e**, Robust adhesion even when the b-MEA is lifted or shaken. $n=12$ independent measurements from 4 biologically independent animals in **b–c**. Values in **b–c** represent the mean \pm s.d. Statistical significance and P values are determined by two-sided Student's t -test at a significance level of 0.05. ns indicates no statistically significant differences.



Extended Data Fig. 7 | Electrogram signals of ventricular fibrillation from an MEA with BTIM encapsulation. a, Representative electrogram signal collected from a Langendorff-perfused rabbit heart during ventricular fibrillation (VF). **b, c**, Phase (**b**) and voltage (**c**) map of VF over 2500 ms.

Reporting Summary

Nature Research wishes to improve the reproducibility of the work that we publish. This form provides structure for consistency and transparency in reporting. For further information on Nature Research policies, see our [Editorial Policies](#) and the [Editorial Policy Checklist](#).

Statistics

For all statistical analyses, confirm that the following items are present in the figure legend, table legend, main text, or Methods section.

n/a Confirmed

- The exact sample size (n) for each experimental group/condition, given as a discrete number and unit of measurement
- A statement on whether measurements were taken from distinct samples or whether the same sample was measured repeatedly
- The statistical test(s) used AND whether they are one- or two-sided
Only common tests should be described solely by name; describe more complex techniques in the Methods section.
- A description of all covariates tested
- A description of any assumptions or corrections, such as tests of normality and adjustment for multiple comparisons
- A full description of the statistical parameters including central tendency (e.g. means) or other basic estimates (e.g. regression coefficient) AND variation (e.g. standard deviation) or associated estimates of uncertainty (e.g. confidence intervals)
- For null hypothesis testing, the test statistic (e.g. F , t , r) with confidence intervals, effect sizes, degrees of freedom and P value noted
Give P values as exact values whenever suitable.
- For Bayesian analysis, information on the choice of priors and Markov chain Monte Carlo settings
- For hierarchical and complex designs, identification of the appropriate level for tests and full reporting of outcomes
- Estimates of effect sizes (e.g. Cohen's d , Pearson's r), indicating how they were calculated

Our web collection on [statistics for biologists](#) contains articles on many of the points above.

Software and code

Policy information about [availability of computer code](#)

Data collection

Fig. 1f, Fig. 6h-i, Extended Data Fig. 7b and Supplementary Fig. 30 used MICAM05 system (SciMedia) and Intan recording system (Intan Technologies).
 Fig. 2b-c, Supplementary Fig. 5c-d and Supplementary Fig. 6e used MTS Sintech 20G system (MTS).
 Fig. 2d, Supplementary Fig. 9 and Supplementary Fig. 10 used ABAQUS Analysis User's Manual 2010 V6.10 (ABAQUS).
 Fig. 2e and Supplementary Fig. 13d used the RheoCompass software (Anton Paar GmbH).
 Fig. 2f and Supplementary Fig. 12 used LEXT OLS5000 v1.3.2.144 (Olympus).
 Fig. 2i-k Extended Data Fig. 3 and Extended Data Fig. 4 used COMSOL Multiphysics v5.2a (COMSOL).
 Fig. 2m, Extended Data Fig. 1f-k, Extended Data Fig. 2f, Supplementary Fig. 17f-g, Supplementary Fig. 18, Supplementary Fig. 24b, Supplementary Fig. 31k and Supplementary Fig. 32b-c used AutoLab NOVA v2.1.4 (Metrohm AG).
 Fig. 3e, Fig. 4c-d, Extended Data Fig. 5b-c, and Supplementary Fig. 19b used microCT digital monitoring system (Mediso-USA) and MR-compatible physiologic monitoring system (SA Instruments).
 Fig. 3k and Extended Data Fig. 6b-c used Olympus VS120 system (Olympus Scientific Solutions Americas).
 Fig. 4i and Supplementary Fig. 16 used UV WinLab software for UV/Vis software (PerkinElmer).
 Fig. 5f-g used an EVOS Imaging system (Thermo Fisher Scientific).
 Fig. 5h-j, Fig. 6b, Fig. 6f-g, Extended Data Fig. 7a, Supplementary Fig. 28 and Supplementary Fig. 29 used the PowerLab acquisition system and LabChart software v8.1.13 (AD Instruments).
 Extended Data Fig. 2a and Extended Data Fig. 2c-d used WinCadence 5.4.0.5 (Physical Electronics).
 Extended Data Fig. 2e used EASE 3.01D (J.A. Woollam).
 Supplementary Fig. 1b used Bruker TopSpin 3.6.2 (Bruker).
 Supplementary Fig. 1c-d used flexAnalysis 3.4 (Bruker).
 Supplementary Fig. 14d used Gen5 software (BioTek Instruments) to capture images.
 Supplementary Fig. 20 used Raspberry Pi Camera v2 (Raspberry Pi Foundation) for video acquisition.

Data analysis

Fig. 1f, Fig. 6h-i, Extended Data Fig. 7b and Supplementary Fig. 30 were analyzed using a custom MATLAB software called "RHYTHM" which is freely available on GitHub. Optical mapping data analysis software is openly available at <https://github.com/optocardiography>. Fig. 1f, 6h, 6i and Extended Data Fig. 7 used the lineshape fitting in a custom MATLAB R2019b program (MathWorks). Fig. 3e, 4c-d, Extended Data Fig. 5b-c, and Supplementary Fig. 19b were reconstructed by filtered (Butterworth filter) back-projection software from Mediso and visualized in Amira v2020.3. The analysis of microCT was performed using Amira v2020.3 software (FEI). Fig. 3k and Extended Data Fig. 6b-c was analyzed by FIJI (ImageJ 1.52p, Schindelin et al., 2012) and a custom MATLAB R2019b program (MathWorks). Fig. 5h-j, 6b, 6f-g, Extended Data Fig. 7a, Supplementary Fig. 28 and Supplementary Fig. 29 was analyzed using LabChart 8 v8.1.13 (AD Instruments). Fig. 5f-g was assessed using a custom MATLAB program (MathWorks). Extended Data Fig. 2a and Extended Data Fig. 2c-d were analyzed by WinCadence 5.4.0.5 (Physical Electronics). Extended Data Fig. 2e was analyzed by EASE 3.01D (J.A. Woollam). Supplementary Fig. 1b was analyzed by Mnova 8.1.4 (Bruker). Supplementary Fig. 1c-d was analyzed by Polytool 2.0 (Bruker). Supplementary Fig. 14d was analyzed using Gen5 software (BioTek Instruments). Supplementary Fig. 20 was analyzed using Toxtrac Version 2.90 (Rodriguez, A., et al., 2018). Statistical analysis of Fig. 3k and Extended Data Fig. 6b-c were performed by Microsoft Excel (Microsoft). Statistical analysis of Fig. 5f-g and Fig. 6f-g were performed by Statsoft (Statsoft). Statistical analysis of Extended Data Fig. 2f were performed by Prism v8.0.1.244 (GraphPad). OriginPro 8.5 were used for data plotting.

For manuscripts utilizing custom algorithms or software that are central to the research but not yet described in published literature, software must be made available to editors and reviewers. We strongly encourage code deposition in a community repository (e.g. GitHub). See the Nature Research [guidelines for submitting code & software](#) for further information.

Data

Policy information about [availability of data](#)

All manuscripts must include a [data availability statement](#). This statement should provide the following information, where applicable:

- Accession codes, unique identifiers, or web links for publicly available datasets
- A list of figures that have associated raw data
- A description of any restrictions on data availability

Source data are provided with this paper. All other data that support the results in this study are available from the corresponding authors on reasonable request.

Field-specific reporting

Please select the one below that is the best fit for your research. If you are not sure, read the appropriate sections before making your selection.

Life sciences Behavioural & social sciences Ecological, evolutionary & environmental sciences

For a reference copy of the document with all sections, see [nature.com/documents/nr-reporting-summary-flat.pdf](https://www.nature.com/documents/nr-reporting-summary-flat.pdf)

Life sciences study design

All studies must disclose on these points even when the disclosure is negative.

Sample size

The work was an explorative proof-of-concept; therefore, we did not pre-determine the sample sizes needed for significance. Sample sizes were 6 biologically independent animals for "+ Adhesion" group and 3 biologically independent animals for "-Adhesion" group in Fig. 3a-h. Sample size was 4 biologically independent animals in Fig. 3i-k, Fig. 4e-f, Supplementary Fig. 14a-d and Supplementary Fig. 21d. Sample size was 3 biologically independent animals in Fig. 4a-d, Fig. 5a-g, Extended Data Fig. 5, Supplementary Fig. 14e-g, Supplementary Fig. 15 and Supplementary Fig. 21 a-c. Sample sizes were 11 independent electrodes in Fig. 6f and 16 independent electrodes in Fig. 6g. Sample size was 12 independent measurements from 4 biologically independent animals in Extended Data Fig. 6b-c. Sample size was 8 independent animals in Supplementary Fig. 20.

Statistical significance and P values of Fig. 3k, Extended Data Fig. 6b-c, Supplementary Fig. 17 and Supplementary Fig. 18 were determined by two-sided Student's t-test.

Statistical significance and P values of Fig. 5f-g were determined by Kruskal-Wallis test and Post-hoc Dunn's multiple comparison test.

Statistical significance and P values of Fig. 6f-g were determined by Wilcoxon matched pairs signed-rank test.

Statistical significance and P values of Extended Data Fig. 2f were determined by one-way ANOVA.

Data exclusions

The following animals were excluded: Animals that did not survive the surgery, animals that opened the sutured incision and animals with defective samples.

Replication

All experiments were replicated based on the sample sizes from independent samples and biologically independent animals, performing on separated days.

Randomization

All devices and animals tested were selected randomly.

Blinding

Investigators involved in the clinical-scoring (Fig. 5f and Supplementary Fig. 15) were blinded.

All histological assessments were double-blinded. Personnel completing quantitative analysis of the H&E stained or Masson's trichrome stained tissue were blinded to group allocations.
Blinding was not relevant to other work since the metrics were quantified and objectively analyzed.

Reporting for specific materials, systems and methods

We require information from authors about some types of materials, experimental systems and methods used in many studies. Here, indicate whether each material, system or method listed is relevant to your study. If you are not sure if a list item applies to your research, read the appropriate section before selecting a response.

Materials & experimental systems

- | | |
|-------------------------------------|---|
| n/a | Involved in the study |
| <input type="checkbox"/> | <input checked="" type="checkbox"/> Antibodies |
| <input type="checkbox"/> | <input checked="" type="checkbox"/> Eukaryotic cell lines |
| <input checked="" type="checkbox"/> | <input type="checkbox"/> Palaeontology and archaeology |
| <input type="checkbox"/> | <input checked="" type="checkbox"/> Animals and other organisms |
| <input checked="" type="checkbox"/> | <input type="checkbox"/> Human research participants |
| <input checked="" type="checkbox"/> | <input type="checkbox"/> Clinical data |
| <input checked="" type="checkbox"/> | <input type="checkbox"/> Dual use research of concern |

Methods

- | | |
|-------------------------------------|---|
| n/a | Involved in the study |
| <input checked="" type="checkbox"/> | <input type="checkbox"/> ChIP-seq |
| <input checked="" type="checkbox"/> | <input type="checkbox"/> Flow cytometry |
| <input checked="" type="checkbox"/> | <input type="checkbox"/> MRI-based neuroimaging |

Antibodies

Antibodies used

Primary antibody for evaluation of biocompatibility in brain:
Rabbit anti-GFAP (1:1000, ab7260, Abcam, Cambridge, UK)
Rabbit anti-IBA1 (1:1000, ab178846, Abcam, Cambridge, UK)
Rabbit anti-Hemoglobin subunit alpha (1:500, ab92492, Abcam, Cambridge, UK)
Secondary antibody for evaluation of biocompatibility in brain:
Goat anti-rabbit Alexa Fluor 647 secondary antibody (1:500, A21244, Thermo Fisher Scientific, MA, USA)

Primary antibody for immunohistochemical staining of dorsal subcutaneous tissues:
Rabbit anti-CD68 antibody (0.5%, ab125212, Abcam, Cambridge, UK)
Rabbit anti-CD163 antibody (0.5%, ab182422, Abcam, Cambridge, UK)

Secondary antibody for immunohistochemical staining of dorsal subcutaneous tissues:
Goat anti-mouse Alexa Fluor 488 (1:500, ab150113, Abcam, Cambridge, UK)
Goat anti-rabbit Alexa Fluor 568 (1:500, ab175471, Abcam, Cambridge, UK)

Validation

All antibodies are commercially available and validated in multiple studies. Complete information is available in the data sheets on the manufacturer's website.

Rabbit anti-GFAP (ab7260, Abcam): This polyclonal antibody recognizes GFAP. Manufacturer-validated to react with mouse and rat GFAP. (<https://www.abcam.com/gfap-antibody-ab7260.html>)

Rabbit anti-IBA1 (ab178846, Abcam): This monoclonal antibody recognizes IBA1. Manufacturer-validated to react with mouse, rat and human IBA1. (<https://www.abcam.com/iba1-antibody-epr16588-ab178846.html>)

Rabbit anti-Hemoglobin subunit alpha (ab92492, Abcam): This monoclonal antibody recognizes Hemoglobin subunit alpha. Manufacturer-validated to react with mouse, rat and human Hemoglobin subunit alpha. (<https://www.abcam.com/hemoglobin-subunit-alpha-antibody-epr3608-ab92492.html>)

Goat anti-rabbit Alexa Fluor 647 (A21244, Thermofisher) secondary antibody: This polyclonal secondary antibody conjugates to Alexa Fluor™ 647. Manufacturer-validated to react with rabbit antibodies. (<https://www.thermofisher.com/antibody/product/Goat-anti-Rabbit-IgG-H-L-Cross-Adsorbed-Secondary-Antibody-Polyclonal/A-21244>)

Rabbit anti-CD68 antibody (ab125212, Abcam): This polyclonal antibody recognizes CD68. Manufacturer-validated to react with mouse and rat CD68. (<https://www.abcam.com/cd68-antibody-ab125212.html>)

Rabbit anti-CD163 antibody (ab182422, Abcam): This monoclonal antibody recognizes CD163. Manufacturer-validated to react with mouse, rat and human CD163. (<https://www.abcam.com/cd163-antibody-epr19518-ab182422.html>)

Goat anti-mouse Alexa Fluor 488 (ab150113, Abcam): This polyclonal secondary antibody conjugates to Alexa Fluor™ 488. Manufacturer-validated to react with mouse antibodies. (<https://www.abcam.com/goat-mouse-igg-hl-alex-fluor-488-ab150113.html>)

goat anti-rabbit Alexa Fluor 568 (ab175471, Abcam): This polyclonal secondary antibody conjugates to Alexa Fluor™ 568. Manufacturer-validated to react with mouse antibodies. (<https://www.thermofisher.com/order/catalog/product/A31634?SID=srch-hj-A31634#/A31634?SID=srch-hj-A31634>)

Eukaryotic cell lines

Policy information about [cell lines](#)

Cell line source(s)	L-929 mouse cells were purchased from ATCC.
Authentication	Cell lines were authenticated by ATCC.
Mycoplasma contamination	Not performed.
Commonly misidentified lines (See ICLAC register)	No commonly misidentified cell lines were used.

Animals and other organisms

Policy information about [studies involving animals](#); [ARRIVE guidelines](#) recommended for reporting animal research

Laboratory animals	<p>Studies on skin, dorsal subcutaneous tissues, and brain tissue: Male and female C57BL/6 mice from Charles River Laboratories weighing ~20 grams, 60–80 days old at the time of implant.</p> <p>Studies on long term cardiac implantation: Male and female Sprague Dawley or Long Evans rats weighing 300–600 grams, 10–12 weeks old at the time of implant.</p> <p>Studies on adhesion of mapping array: Female New Zealand white rabbit, weighing ~3 kg, 3 months old at the time of experiment.</p>
Wild animals	The study did not involve wild animals.
Field-collected samples	This study did not involve samples collected from the field.
Ethics oversight	<p>The mouse work was performed under the study protocol #IS00000707, as approved by the Institutional Animal Care and Use Committee of Northwestern University.</p> <p>The rat work was performed under the study protocol #A364 as approved by the Institutional Animal Care and Use Committee of The George Washington University.</p> <p>The rabbit work was performed under the study protocol #A327 as approved by the Institutional Animal Care and Use Committee of The George Washington University.</p> <p>All protocols are conformed to guidelines as suggested by the Guide for the Care and Use of Laboratory Animals published by the National Institutes of Health.</p>

Note that full information on the approval of the study protocol must also be provided in the manuscript.